Editor's Summary

Coordinating cell wall synthesis and cell division

Most bacteria are protected by peptidoglycan cell walls, which must be remodeled to split the cell. Cell division requires the tubulin homolog FtsZ, a highly conserved cytoskeletal polymer that specifies the future site of division. Bisson-Filho *et al.* and Yang *et al.* found that the dynamic treadmilling of FtsZ filaments controls both the location and activity of the associated cell wall synthetic enzymes. This creates discrete sites of cell wall synthesis that circle around the division plane to divide the cell.

Science, this issue p. 739, p. 744

www.sciencemag.org/content/355/6326/744/suppl/DC1

Supplementary Materials for

GTPase activity–coupled treadmilling of the bacterial tubulin FtsZ organizes septal cell wall synthesis

Xinxing Yang, Zhixin Lyu, Amanda Miguel, Ryan McQuillen, Kerwyn Casey Huang,*
Jie Xiao*

*Corresponding author. Email: kchuang@stanford.edu (K.C.H.); xiao@jhmi.edu (J.X.)

Published 17 February 2017, *Science* **355**, 744 (2017)
DOI: 10.1126/science.aak9995

This PDF file includes:

Other supplementary material for this manuscript includes the following:

Materials and Methods

Strains and plasmids

Plasmids expressing GFP-tagged FtsZ mutants ($P_{T5\text{-}lac}$::*ftsz^{mut}-gfp*, pXY033, pXY035, pXY036, pXY040, pXY054, and pXY092) were constructed via site-directed mutagenesis from the *ftsZ^{WT}*-expressing pXY021 as previously described in (*11*) using primers 1-14 (Table S6).

Plasmid pJB007 ($P_{T5\text{-}lac}$::*TagRFP-t-ftsI*, *cat*) was constructed by amplifying the *TagRFP-t* (a gift from Dr. R. Y. Tsien) (*37*) and *ftsI* genes from PVS155-FtsI (*15*), using primers 24 and 25, and 26 and 27, respectively (Table S6). The amplified *TagRFP-t* and *ftsI* genes were digested by SpeI and EcoRI, and EcoRI and SalI, respectively. The backbone vector pCH027 (*15*) was linearized by SpeI and ligated with *TagRFP-t* and *ftsI*.

Plasmid pRM006 ($P_{T7\text{-}lac}$::*His-sumo-ftsZ^{WT}*) was created by first amplifying the *ftsZ* gene from pJB041 ($P_{T7\text{-}lac}$::*His-TEV-ftsZ^{WT}*) (*27*) using primers 15 and 16 (Table S6). Next, the amplified *ftsZ* gene product and pTB146 ($P_{T7\text{-}lac}$::*His-sumo*, a gift from Dr. E. Goley) were digested using EcoRI and SalI and subsequently ligated to create plasmid pRM006 for FtsZ expression and purification.

Plasmids expressing His-SUMO tagged FtsZ^{mut} for purification ($P_{T7\text{-}lac}$::*His-sumo-ftsZ^{mut}*, pXY142, pXY148, pXY194, pXY195, pXY196, pXY197, and pXY198) were constructed by site-directed mutagenesis of pRM006 using primers 1-14 (Table S6).

Plasmid PXY104 (P_{BAD}::*ftsZ-GFP, spec^{R}*) was created by amplifying *ftsZ-gfp* from pXY21 using primers 28 and 29 (Table S6). The amplified product and backbone vector PJB066 (*13*) were digested using NheI and PstI and ligated.

FtsZ^{mut} strains XY058, XY072, XY075, XY076, XY077, XY088, XY089, XY129 (Table S6) were constructed by replacing the chromosomal *ftsZ* locus of *E. coli* BW25113 with *ftsZ^{mut}* alleles using λ-red homologous recombination (*38*). *ftsZ^{mut}* alleles were first amplified from $P_{T5\text{-}lac}$::*ftsZ^{mut}-gfp* using primers 17 and 18 (Table S6). The *kan^{R}* antibiotic resistance marker was amplified from plasmid pKD3 (gift from B. L. Wanner, Addgene plasmid #45604) using primers 19 and 20 (Table S6). The two fragments with 20-bp overlaps were amplified and fused to create the full fragment *ftsZ^{mut}-frt-kan-frt* using primers 17 and 22 and fusion PCR (Table S6). This fragment was used to transform BW25113 cells containing the pKD46 plasmid with 0.2% L-arabinose induction. Recombinants grown on LB + kanamycin plates were verified by colony PCR using primers 22 and 23 (Table S6). The pKD46 plasmid was then cured by reinoculating and restreaking multiple times in the absence of ampicillin at 30 °C. We employed the strategy of losing the pKD46 plasmid by natural dilution to avoid the use of high temperatures, as most FtsZ mutants are temperature sensitive (*19*). The PCP20 plasmid was then used to transform these strains, and induced to flip out the *kan^{R}* cassette. PCP20 was then subsequently cured using the same dilution method as for pKD46. The final strains were verified by sequencing the colony-PCR product of primers 22 and 23 (Table S6). The strains were then transformed with the plasmids expressing the appropriate FtsZ^{mut}-GFP for imaging.

BW25113 *ftsZ*::*ftsZ$^{55\text{-}56}$-msfGFP* (KC606) was constructed using P1 transduction of an MG1655 strain bearing *ftsZ$^{55\text{-}56}$-msfGFP::cat* at the chromosomal *ftsZ* locus (KC555).

The two-color FtsZ-FP strain (XY236) was created by transformation of BW27783 *ftsZ*::*ftsZ$^{55\text{-}56}$-mNeonGreen* (a gift from Dr. H. Erickson (*14*)) with P_{lac}::*ftsZ-TagRFP-T* (pCH033) (*11*).

Whole genome sequencing

BW25113 parental and FtsZ^{mut} strains were grown to OD_{600}~0.7 to prepare chromosomal DNA using a DNeasy Blood & Tissue Kit (Qiagen). Whole genome sequencing was performed on a MiSeq platform with the 2X300 v3 kit (Illumina). Short (200-bp), paired reads were aligned against the reference genome (*E. coli* K12 strain DH10B) using the MiSeq automated analysis pipeline to find single nucleotide variants. The extra variants of FtsZ^{mut} strains that passed the quality test and differed from the parental strain are listed in Table S4.

Growth conditions

For Western blots, scanning electron microscopy, time-lapse fluorescence imaging, fluorescence recovery after photobleaching (FRAP), Structured Illumination Microscopy (SIM) imaging and HADA labeling studies, cells were grown as previously described (*11*), with some modifications. Briefly, overnight cultures grown in LB were diluted by at least 1:100 in M9 medium supplemented with MEM vitamins, MEM amino acids, and 0.4% glucose (hereafter referred to as M9 unless otherwise indicated), and grown at 30 °C overnight (the D212G and D212A strains required an additional 8-12 h to reach the same OD_{600} as the other strains). The cultures were then diluted 1:50 into M9 for overnight growth at room temperature to OD_{600} ~0.3-0.6. Antibiotics were included in all cultures at concentrations of 50 μg/mL for kanamyicin, 75 μg/mL for chloramphenicol, and 50 μg/mL for ampicillin when appropriate. Before imaging, cells were washed twice with fresh M9.

For single-molecule tracking of FtsZ or FtsI, cells were grown directly in M9 media from single colonies to minimize the protein concentration by avoiding the auto-induction effect that occurs in LB.

For drug-treated time-lapse imaging and HADA labeling, a stock of A22 (20 mg/mL), mecillinam (20 mg/mL), cefsulodin (20 mg/mL), cephalexin (14 mg/mL), or combinations of A22 (20 mg/mL) and cephalexin (14 mg/mL), was added to cells (OD_{600} ~ 0.3–0.4) grown in M9 at a final concentration of 200 μg/mL. Cells were allowed to grow for two more hours (approximately one division period) in M9 at room temperature before time-lapse imaging or HADA labeling.

Protein purification

Plasmids bearing His-SUMO-tagged *ftsZ^{WT}* and *ftsZ^{mut}* genes (Table S6) were transformed and overexpressed in Rosetta (DE3) pLysS *E. coli* cells (a gift from Dr. E. Goley). 1 L of cell culture was grown at 30 °C for 3-4 h to OD_{600}~0.6 and induced with 1 mM IPTG for 4 h. Cells were harvested by centrifugation at 6,000*g* for 15 min at 4 °C and resuspended in 40 mL pre-chilled Buffer A (50 mM Tris, pH 8, 50 mM KCl, 20 mM imidazole, 1% sucrose). The suspensions were snap-frozen using ethanol-dry ice and stored at -80 °C.

For purification, cell suspensions were thawed at 37 °C. 1 mg/mL lysozyme, 2 mM phenylmethyl sulphonyl fluoride (PMSF) and 2 units/mL DNAse I (New England Biolabs) final concentration were added to the suspensions. Each suspension was incubated at room temperature for 30 min followed by 10 s sonication six times on ice. Cell lysates were then diluted 1:1 by volume in Buffer A with 0.5 mM EDTA and incubated with rotation at room temperature for 30 min. This step effectively increased the yield of some FtsZ variants with low GTPase activity, such as D212G and D158A. Cell lysates were spun down at 15,000*g* for 30 min and filtered by passing through a 0.22-μm filter (Millex-GV, Merck Millipore Ltd.). Supernatants were loaded onto 5 mL ProBond Nickle-Chelating Resin (Novex, Thermo Scientific Inc) and washed with Buffer B (50 mM Tris, pH 8, 50 mM KCl, 30 mM imidazole, 1% sucrose). Bound protein was eluted by buffer C (50 mM Tris, pH 8, 50 mM KCl, 300 mM imidazole, 1% sucrose). Peak fractions were combined and the concentrations were estimated by OD_{280}. His-Ulp1 (SUMO protease, a gift from Dr. E. Goley) was added 1:200 (molar ratio) to the combined protein fractions. The resulting reaction mixtures were dialyzed against Buffer A overnight at 4 °C, subsequently loaded onto 2 mL ProBond Nickle-Chelating Resin,

and washed with the same volume of Buffer A. The flow-through and wash fractions were combined and dialyzed against MES polymerization buffer (pH 6.5, 50 mM MES, 50 mM KCl, 2.5 mM $MgCl_2$, 1 mM EGTA, 1% sucrose) overnight at 4 °C. The combined fraction was concentrated to ~1 mL with a Vivaspin 30000 MWCO (GE lifescience), sucrose was added to a final concentration of 10%, and aliquots were snap-frozen at -80 °C. FtsZ protein concentrations were measured using the BCA assay (Thermo Scientific Inc #23250).

GTPase assays

The GTPase activities of WT and mutant FtsZ proteins were measured using the Pyruvate Kinase/Lactic Dehydrogenase (PK/LDH) assay as previously described (*18*). All measurements were performed in MES polymerization buffer with 500 μM NADH, 2 mM phosphoenolpyruvate, 6-9.3 units/mL lactose dehydrogenase and 4-6.6 units/mL pyruvate kinase (pre-mixed, Sigma-Aldrich, P0294). An Agilent Cary 60 UV-Vis spectrophotometer coupled with a PCB1500 temperature controller was used to measure the GTPase activity of $FtsZ^{WT}$ and $FtsZ^{mut}$ proteins at 23 °C, which is the same temperature used for live-cell imaging. 5 μM $FtsZ^{WT}$ or 10 μM $FtsZ^{mut}$ protein was premixed with the MES polymerization buffer and allowed to stand to reach steady state in the spectrophotometer for 10 min. A small volume (1-3 μL) of GTP at high concentrations (1, 10, or 100 mM) was added into the cuvette at a final concentration from 10 μM to 2 mM to initiate the reaction. GTP hydrolysis rates of each FtsZ mutant at different GTP concentrations were calculated from the slopes of the linear decrease of NADH absorbance at 340 nm, and were fit with a Hill-modified Michaelis-Menten equation (*18*)

$$V_{\mathrm{GTPase}} = \frac{k_{\mathrm{cat}}[\mathrm{FtsZ}][\mathrm{GTP}]^n}{K_m^n + [\mathrm{GTP}]^n}$$

to obtain k_{cat} and K_{m} values for each FtsZ variant (fig. S8A, Table S1). Note that the GTP hydrolysis activities (k_{cat}) we measured are generally lower than previously reported values (*19, 39*), which is likely due to differences in experimental conditions, including the method for FtsZ purification and polymerization, detection of phosphate release, and temperature. For example, we observed a strong temperature dependence of the GTPase activity of $FtsZ^{WT}$ (measured with 4 mM GTP at 23 °C, 30 °C and 37 °C; fig. S8A) and the activities at 30 or 37 °C were comparable with previous results (*5, 18, 40*). Thus, it is important to note that the relative differences in GTPase activity between $FtsZ^{WT}$ and $FtsZ^{mut}$ proteins we observed were determined under identical conditions.

Quantitative immunoblotting

Cells were harvested by centrifugation at OD_{600}~0.3, resuspended in SDS gel-loading buffer, and boiled at 100 °C for 5 min. Whole-cell extracts were applied to a 10% SDS-PAGE gel and electroblotted onto nitrocellulose membranes. After blocking in TBS with 0.05% (v/v) Tween-20 and 5% (w/v) non-fat dry milk, membranes were incubated with rabbit anti-FtsZ antibody (a gift from Dr. H. Erickson), and diluted 1:4500 in TBS with 0.05% (v/v) Tween-20 and 1% (w/v) BSA. FtsZ bands were detected using goat anti-rabbit HRP (1:45,000 dilution; Bio-Rad) and Clarity TM Western ECL Substrate (Bio-Rad). Band intensities were quantified using ImageJ and used to calculate the fraction of FtsZ-GFP relative to total cellular FtsZ levels (fig. S2).

Complementation of TagRFP-T-FtsI in an FtsI temperature sensitive strain

Plasmid pJB007 carrying the *tagRFP-t-ftsI* fusion gene was used to transform a temperature-sensitive FtsI strain MCI23 (MC4100 *ftsI23(ts) leu-260::Tn10*, a gift from Dr. J. Lutkenhaus) (*41*). Transformants were verified by sequencing, and inoculated in LB medium containing chloramphenicol (75 μg/mL) and streptomycin (50 μg/mL), for overnight growth at 30 °C. After the OD_{600} reached ~0.1), 3 μL of serial dilutions (10- to 100,000-fold) of the culture, together with the

parental strain MC123 and the wild-type control strain MC4100 grown under the same condition, were spotted onto an LB plate, incubated overnight at 42 °C, and photographed (fig. S15).

Scanning electron microscopy (SEM)

SEM imaging was performed as previously described (*11, 15*). BW25113 WT and FtsZ^{mut} cells were cultured to OD_{600}~0.6 in M9, concentrated, washed with M9, and then applied directly to 0.01% poly-L-lysine (PLL)-treated coverslips (0.01% PLL for 10 min, 5 min dH_2O wash). Cells were fixed on the coverslip using 2% formaldehyde, 2% glutaraldehyde, 0.08 M Sorenson's Phosphate Buffer (SPB), 3 mM MgCl2, pH 7.2. Cells were then post-fixed in 0.8% potassium ferrocyanide-reduced 1% OsO4 in 0.08 M SPB and 3 mM $MgCl_2$, and incubated on ice in the dark for 1 h. Coverslips with fixed cells were coated with 10-20 nm AuPd via a Denton Vacuum Desk II sputter coater, and imaged on a Leo1540 FESEM operating at 1kV (Fig. 3A and fig. S12).

TIRF time-lapse fluorescence imaging and analysis

Time-lapse fluorescence imaging of FtsZ-GFP and GFP-ZapA was performed on an Olympus IX-71 inverted microscope (1.45 NA 60X TIRF objective, 1.6X magnification enabled) with an Andor iXon-DU897 camera as described in (*13*). The objective-based TIRF illumination was achieved by shifting the expanded 488-nm laser beam (Coherent Sapphire 488) off the optical axis center. The TIRF imaging angle was measured with a 20-mm right-angle prism (refractive index = 1.518, Thorlabs PS908) and fixed at ~70°. The incident excitation power at 488 nm was adjusted to 5W/cm^2 by a neutral density filter (Thorlabs) to minimize photobleaching. The frame rate for periodic dynamics of FtsZ-GFP was set at 1 frame/s for all FtsZ variants except D212A and D212G, for which the frame rate was 0.5 frame/s. The exposure time was set at 140 ms. These imaging settings were chosen to minimize photobleaching in order to acquire long time traces (~600 to 1200 s) for PSD analysis. For drug-treated conditions, the drug was mixed into the imaging gel-pad at the same concentration (200 μg/mL) as in liquid cultures, and imaged within two hours. To monitor treadmilling dynamics, a frame rate of 2 frame/s and a 1.49 NA 100X TIRF objective were used to achieve higher temporal and spatial resolutions. In general, treadmilling traces were shorter (200 s) because photobleaching of GFP was significant due to the faster frame rate, and hence the traces became unsuitable for PSD analysis. Two-color FtsZ dynamics were monitored by exciting the XY236 strain with both 488-nm (5W/cm^2) and 561-nm (250W/cm^2) lasers simultaneously. The fluorescence was split by a T570-lpxr dichroic splitter (Chroma) with ET525/50 and ET630/70 emission filters. The two-channel images were registered using TetraSpec microsphere beads (Thermo Fisher).

Analysis of Z-ring intensity fluctuations during time-lapse imaging was performed with custom Matlab scripts. Cells without significant constriction but stable FtsZ-ring were selected for PSD analysis. Briefly, a cell of interest was cropped out from both fluorescence and bright-field images. Fluorescence images were registered to the corresponding bright-field images to account for sample/stage drift during the time-lapse. Second, the cell was rotated manually to align the Z-ring horizontally. Fluorescence background within the cell was calculated by averaging the total integrated intensity over the area defined by the cell contour. A square region of interest (ROI) with 3×3 pixels (~500 nm) in the center of the ring was then chosen manually. The local FtsZ-GFP intensity, $I_r(t)$, was calculated as the integrated intensity within the ROI after background subtraction.

Treadmilling analysis was performed to cells with and without stable FtsZ-ring using the ImageJ kymograph plugin (http://www.embl.de/eamnet/html/body_kymograph.html, J. Rietdorf and A. Seitz, EMBL, Heidelberg). Fluorescence images of individual cells were cropped, corrected for photobleaching, interpolated to 20 nm/pixel via the bicubic method in ImageJ, and moving-averaged over a 4-frame window of time. The fluorescence intensity of an FtsZ polymer along the direction of its movement in each frame was determined from the intensity along a line with a

width of 11 interpolated pixels (~200 nm) manually drawn across the full length of the path of the FtsZ polymer. This line was then used to plot the kymograph (Fig. 2A,B). The polymerization and depolymerization speeds of the polymer were calculated by manually measuring the slopes of the leading and trailing edges of the fluorescence zigzags in the kymograph (Fig. 2C, D). The treadmilling speed (Fig. 2G) was calculated as the average of the absolute speeds of polymerization and depolymerization.

Directional movement of TagRFP-T-FtsI

TagRFP-T-FtsI tracking was performed on the similar optical set up as FtsZ treadmilling imaging (an Olympus IX-71 inverted microscope equipped with a 1.49 NA 100X TIRF objective, 1.6X magnification enabled, and an Andor iXon-DU897 camera), but in epifluorescence-illumination mode using a 561-nm laser (Coherent Sapphire). The epi-illumination mode enabled imaging of FtsI molecules in constricting cells, which was difficult in TIRF mode. TagRFP-T-FtsI molecules were tracked continuously with 1-s exposure time for 100-200 s with a laser power of ~1 W/cm^2. The long exposure time blurs the fast diffusion of mobile FtsI molecules on the cylindrical part of the cell, and hence allows visualization of slow-moving FtsI molecules at the septa as bright fluorescent spots. Only cells with distinct, septum-localized TagRFP-T-FtsI fluorescence spots were selected for analysis. We note that many FtsI molecules away from the septa were observed to have faster mobility (fig. S11B, Movie S17); these molecules are expected not to be involved in division based on their spatial localization. Cells expressing high levels of TagRFP-T-FtsI determined by the overall cellular fluorescence were not used for analysis, as it was difficult to distinguish clear TagR-T-FtsI spots at the septa. Time-lapse movies were preprocessed in the same manner as FtsZ-treadmilling movies, and the corresponding kymographs were used to measure the speed of directional movement of TagRFP-T-FtsI as with FtsZ-GFP. Tracks formed by single TagRFP-T-FtsI molecules were identified from the formation of diffraction-limited spots in fluorescence images, and by single-molecule blinking and abrupt photobleaching behaviors in time traces (fig. S16).

Single FtsZ-GFP molecules were tracked with similar imaging condition as TagRFP-T-FtsI, except using a 488-nm laser with higher power (4 W/cm^2). Given the higher expression levels of FtsZ, we first excited cells for 600 s to bleach the vast majority of FtsZ-GFP and thereby ensure measurement of single FtsZ molecules (fig. S11).

Fluorescence recovery after photobleaching (FRAP)

FRAP experiments were performed on a home-built Olympus IX-71 inverted microscope as previously described (*13*). Briefly, the excitation laser (488 nm) was split with a combination of a linear polarizer and a polarizing beam-splitting cube to generate two excitation beams, the transmitted photobleaching beam and the reflected epifluorescence illumination beam. The transmitted beam was focused to a diffraction-limited spot on the edge of the Z-ring for photobleaching, while the reflected beam was used to image the cell before and after photobleaching. Images were acquired every 1 s for 4 min after photobleaching, except for the D212G mutant, which was imaged every 8 s for 32 min. The exposure time for all acquisitions was 50 ms. Custom Matlab scripts as described previously (*13*) were used to analyze FRAP curves. Each curve presented in fig. S8C, D was the average of three independent experiments (~20-40 cells in each experiment).

HADA pulse labeling, imaging, and analysis

HADA (HCC-amino-D-alanine) labeling and fixation of cells were performed as previously described (*33*), with some modifications. Briefly, 1 mL of BW25113 cells in M9 media (with/without drug, OD_{600} ~0.6) was spun down at 10,000*g* for 2 min at room temperature and resuspended in 100 µL M9 (with same drug concentration for inhibition experiments). Cells were then mixed by brief vortexing with 1 µL HADA solution (8 mM, a gift from Drs. Y. Brun and M. VanNieuwenhze), and

allowed to grow at room temperature with rocking for different lengths of time (90, 270, 810, and 1800 s). For shorter pulse labeling (10 and 30 s), cells were manually shaken after vortexing. For 1-s pulse labeling, cells were fixed immediately after vortexing. For drug inhibition experiment (fig. S13), the labeling time was 2 min. At the end of labeling pulses, 230 μL pre-chilled 100% ethanol were added to the cell culture and mixed by thorough pipetting to stop the labeling reaction and fix the cells. An additional 1 mL pre-chilled 70% ethanol was added to the tube immediately to further dilute HADA and reduce nonspecific background binding. Cells were then incubated on ice for 15 min. Fixed cells were washed three times with PBS, resuspended in 20-50 μL PBS to a final OD_{600}~4 to achieve an appropriate cell density for imaging, and stored at 4 °C prior to imaging.

Imaging samples were prepared by adding 1 μL of fixed, HADA-labeled cells on a 22 mm × 22 mm cleaned, square cover glass and sandwiched by another clean cover glass. Imaging was performed on an Olympus IX-81 inverted microscope with a 1.3 NA 100X oil-immersion phase-contrast objective with 1.6X magnification enabled. Phase-contrast images were obtained by placing the focal plane in the middle of the cell, and fluorescence images of HADA were obtained by acquiring three consecutive images (for averaging purposes, to increase signal-to-noise level) with 100-ms exposure time and 405-nm laser excitation at 20 W/cm^2. To accommodate the entire dynamic range of HADA labeling intensity with labeling pulses of different lengths, the EM gain of the Andor iXon-DU888 CCD camera was set to 1 (for 1800 s, 810 s, and 270 s labeling pulses), 10 (for 90 s), 30 (for 30 s), 100 (for 10 s), or 300 (for 1 s) to scale the signal within a reasonable range of gray levels. The real signal gain factor was calibrated with measurements on fluorescence beads, and used to calculate the absolute intensity (fig S14).

To calculate the HADA incorporation intensity at constriction sites, cell outlines were determined from phase-contrast images using *Oufti* (*42*) with manual refinement. Total septal HADA incorporation was calculated by manually cropping out the constriction sites and integrating HADA intensity along a 3 pixel-wide (~240 nm) line that fully spanned the short axis of the cell regardless of whether constriction was complete. The integrated intensity was then scaled by the calibrated EM gain factor. Septa at the poles of D212G cells were not used in this measurement. The percentage of incomplete septa in a population of cells was calculated by dividing the number of incomplete septa by the total number of counted septa. Incomplete septa were defined by the presence of non-uniform, asymmetric HADA intensity along the short axis of the cell. Each sample was independently scored three times by two people to avoid biases.

SIM imaging and data analysis

3D-SIM imaging was performed on a Nikon N-SIM system with a 100X 1.49 TIRF objective and Andor iXon DU-897 camera with 200-ms exposure time. A standard 15-plan 3D-SIM (120-nm interval) was collected to reconstruct the 3D structure of the Z ring (Movie S19).

Time-lapse SIM imaging was implemented with 30-ms exposure time and 5-plan 3D-SIM to reduce the acquisition time to 6 s, which was also the time interval between images. The 3D images were projected by maximal intensity to make Movie S14. Some Z-rings aligned parallel with the imaging plane (Fig. 2E) were selected to make the circumferential kymograph in Fig. 2F.

Constriction and elongation rate measurements

The mean constriction rates of $FtsZ^{mut}$ cells were measured as described previously (*11*). Briefly, the initial septal diameter (d_{septa}) was determined from 2D-PALM imaging, and the division time ($t_{division}$) was determined from time-lapse movies. The initiation of constriction was defined as the first frame in phase-contrast imaging showing invagination, and the end as the disappearance of septal FtsZ-GFP fluorescence. The constriction rate (v_c) was calculated as $d_{septa}/t_{division}$. The length of

the same cells at the beginning and end of division was measured from the phase-contrast images, and the elongation rate during cell division (v_{ec}) was then calculated as $\Delta L/t_{division}$.

Purification of sacculi and UPLC analysis of peptidoglycan composition

UPLC samples were prepared as described previously (*43*). Overnight cultures of *E. coli* BW25113 and FtsZ^{D212G} cells were diluted 1:200 in 250 mL LB or M9 and grown at 37 °C to an OD_{600} of 0.7. Cultures were centrifuged at 5,000*g* for 10 min at room temperature and the resulting pellet was suspended in 3 mL of the same media. Cell suspensions were then lysed by boiling in SDS for 3 h. Lysed cell suspensions were ultracentrifuged at 400,000*g* to purify sacculi, which were then digested with muramidase into muropeptides. Samples were pH-adjusted and injected onto a Waters H Class UPLC system equipped with a BEH C18 1.7-µm column (Waters, MA, USA) and eluted with sodium phosphate buffers. Peaks were quantified and identified as particular muropeptide species from their elution times based on (*44*), from which the crosslinking density and strand length were calculated as previously described (*44*).

Calculation of power spectrum density (PSD)

The fluorescence intensity time trace from a single Z-ring, $\boldsymbol{I_r(t)}$, was first shifted by subtracting its mean value $\langle \boldsymbol{I_r(t)} \rangle$. To calculate the PSD curves across frequencies $\boldsymbol{\nu}$, we computed the Fast-Fourier Transform (FFT) using the fft function in Matlab and normalized its square magnitude by the variance:

$$PSD(\nu) = \frac{|\mathrm{FFT}(I_r(t) - \langle I_r(t) \rangle)|^2}{n\Delta t \cdot \mathrm{Var}(I_r(t))}$$

where n is the number of frames of the trace, and Δt is the time interval between two consecutive frames.

The PSD curves of individual cells in each condition/strain were averaged to generate the mean PSD curve. This mean curve was fit using the equation below to obtain the FtsZ exchange rate and Z-ring periodic frequency:

$$A\frac{2k_{\mathrm{ex}}}{(2\pi\nu)^2 + {k_{\mathrm{ex}}}^2} + B\frac{1}{\nu}e^{-\frac{ln(\nu-\nu_o)^2}{2\omega^2}} + C$$

where k_{ex} is the stochastic exchange rate of FtsZ between the Z-ring and cytoplasmic pool (see section on **Stochastic subunit exchange model of FtsZ dynamics** below). A, B, and C are fitting parameters. The second term is a log-normal distribution that empirically matches the periodic dynamic behavior after the subtraction of the first term. The third term represents all of the white noise in the experiment. Each experimental PSD curves was fit by this equation to extract the exchange rate constant, k_{ex}. The peak frequency of the periodic dynamics of FtsZ is defined as the frequency that has the maximal amplitude in the log-normal distribution after subtracting the contribution of stochastic subunit exchange. The mean and standard deviation of the peak frequency were computed by bootstrapping the mean PSD curve 1000 times and determining the corresponding peak frequency in the resulting log-normal distribution.

Simulation of TIRF illumination and estimation of assembly size, polymerization, and depolymerization rates

The TIRF excitation field along the *z*-axis of the imaging plane was simulated as exponential decay from the glass-cell interface: $\boldsymbol{I(z) = I(0)e^{-z/d}}$, where $I(0)$ is the excitation intensity at the glass-cell interface (z = 0). d is the characteristic penetration depth of TIRF illumination, which can be calculated from the TIRF incidence angle, refractive index, and the wavelength. For our imaging conditions, $d \approx 75$ nm.

The Z-ring radius was estimated to be 430 nm (*11, 13*) with a ~60-nm radial thickness (*11*). With such a geometry (fig. S1), we calculated the excitation intensity of the bottom part of the Z-ring resulting from epifluorescence or TIRF illumination.

The number of FtsZ molecules in an *E. coli* cell has been estimated to be ~4000 by quantitative Western immunoblotting under similar conditions used in our experiments (*11, 15*). The percentage of FtsZ molecules residing in the ring was measured to be ~40% in non-constricting cells (*11, 13, 15*). Therefore, the number of FtsZ in the imaging window can be estimated as 4000×0.4/6 = 267; the 1/6 factor is due to the area of the imaging window (fig. S1B). From immunoblotting, the ratio of FtsZ-GFP to total FtsZ (labeled and unlabeled) in WT cells was 46% (fig. S2), giving an estimate of 227 FtsZ-GFP molecules in the imaging window. Given that the average fluorescence intensity in Z-rings was 6957 (fig. S6) for our imaging conditions, we determined that each FtsZ molecule (both FtsZ and FtsZ-GFP) would account for an average of $6957/(227+267) \approx 14$ counts in the fluorescence image. From this number, we converted the fluorescence intensity of each fluorescence peak in the time traces of individual cells to the number of FtsZ molecules (labeled and unlabeled), and estimated the assembly size and the assembly/disassembly rates (Fig. 1A).

Stochastic subunit exchange model of FtsZ dynamics

The stochastic exchange of FtsZ subunits between the Z-ring and the cytoplasmic pool is partially responsible for the observed Z-ring intensity fluctuations in the TIRF imaging window, and hence contributes to the PSD curve. To evaluate this contribution, we established a kinetic model that accounts for the stochastic exchange of FtsZ subunits. The model is based on both in vitro experimental observations (*7*) and a computational biochemical model of FtsZ assembly (*45*).

We first assume that the Z-ring is in a steady state in which the average number of FtsZ molecules (and hence the fluorescence intensity) in the Z-ring remains constant over a relatively long time scale compared to the exchange rate itself (*11*). The entire assembly and disassembly of the Z-ring during the cell cycle is not considered in the model. In addition, we did not incorporate the regulation of Z-ring assembly by other proteins such as MinC or SlmA, as our experimental measurements showed that they have marginal effects on the observed periodic dynamics (Fig. 1G, H, Table S2). For simplicity, we also assumed that FtsZ forms single protofilaments with no significant lateral interactions with each other in the Z-ring.

The FtsZ molecules are divided into three populations: 1) freely diffusing monomers in the cytoplasm, 2) dimers at low concentration that act as protofilament nucleation sites in the Z-ring, from which a new FtsZ protofilament can grow (*7*), and 3) trimers and larger oligomers that are stable within the Z-ring, which are the main contribution to the observed Z-ring intensity.

The concentrations of GTP and GDP are assumed to be constant (5 mM and 0.7 mM, respectively, both of which are much greater than the cellular FtsZ concentration at ~4-5 μM (*15*)). Based on the excess of GTP relative to FtsZ and the fast rate of binding (~12 $\mu M^{-1}\ s^{-1}$ (*40*)), we assume that the GDP to GTP exchange reaction is fast and hence that practically all FtsZ subunits in the cytoplasm can be considered to be GTP-bound.

At steady state, an FtsZ protofilament in the Z-ring can elongate by adding more FtsZ subunits at the ends (polymerization), or ligating with another protofilament. The protofilament can also shorten in length by depolymerizing at one end, or breaking in the middle. The reaction scheme for a protofilament of length *i,* denoted by $(Z \dots Z)_i$, is shown below:

Elongation: $(Z \dots Z)_i + Z \overset{k_E}{\rightarrow} (Z \dots Z)_{i+1}$

Shortening: $(Z \dots Z)_i \overset{k_S}{\rightarrow} (Z \dots Z)_{i-1} + Z$

Breakage: $(Z \dots Z)_i \overset{k_B}{\rightarrow} (Z \dots Z)_m + (Z \dots Z)_n,\ m+n=i,\ m>2, n>2$

Ligation: $(Z \dots Z)_k + (Z \dots Z)_l \overset{k_L}{\rightarrow} (Z \dots Z)_i,\ k+l=i,\ k>2, l>2$

Nucleation: $Z + Z \overset{k_N}{\rightarrow} (ZZ)_2$

*Elongation and shortening only happen at the end of a protofilament.

where k_E, k_S, k_B, k_L, and k_N are rate constants for the elongation, shortening, breakage, ligation, and nucleation steps. Note that k_B and k_S are dependent on the GTP hydrolysis rate since the GDP interface is less stable in an FtsZ protofilament (*46*).

According to this model, FtsZ protofilaments in the Z-ring are a mixture of different lengths *i*. Instead of using multiple species of FtsZ protofilaments with different lengths *i*, the system can be described using the following variables: total number of FtsZ in the Zring (Z_t), total number of FtsZ protofilaments (n_p), total number of FtsZ-FtsZ interfaces (n_{in}), and total number of FtsZ at the ends of protofilaments (n_{end}). These four quantities are not independent, with $n_{\text{in}} = Z_t - 3n_p$ and $n_{\text{end}} = 2n_p$. The reaction equations can then be written as

$$\frac{dZ_t}{dt} = -k_S n_{\text{end}} + k_E n_{\text{end}} Z_{\text{free}} + 2k_N Z_{\text{free}}^2 \quad (1)$$

$$\frac{dn_p}{dt} = -k_L n_p^2 + 2k_B n_{\text{in}} + k_N Z_{\text{free}}^2 \quad (2)$$

where the terms on the right-hand sides represent shortening, elongation, and nucleation (Eq. 1), and ligation, breakage, and nucleation (Eq. 2), respectively. The number of FtsZ molecules in the cytoplasm (Z_{free}) is equal to the total number of FtsZ minus the number in the ring, $Z_t - Z_r$.

Assuming that the nucleation rate $k_N Z_{\text{free}}^2$ is negligible (*7*), a nullcline analysis of Eqs. 1 and 2 indicated that the steady-state (ss) concentration of FtsZ in the Z-ring is

$$Z_{t,ss} = \frac{k_E Z_t - k_S}{k_E} \quad (3)$$

and the number of FtsZ protofilaments at steady state is

$$n_{p,ss} = \frac{-3k_B + \sqrt{9k_B^2 + 4k_L k_B (Z_t - k_S/k_E)}}{2k_L} \quad (4)$$

To calculate the PSD of the steady-state intensity fluctuations, we first calculated the autocorrelation function. Random fluctuations such as photon and detection noise do not contribute to the average autocorrelation function. Thus, all of the correlation arises from the

kinetic fluctuations dictated by the reactions described in Eqs. 1 and 2. Here, we define the autocorrelation function as the intensity correlation

$$C_I(\tau) = Q^2 C_Z(\tau) = Q^2\langle \delta Z_t(0)\delta Z_t(\tau)\rangle \tag{5}$$

where Q is the product of excitation power, quantum yield, and detection coefficient, which represents the brightness of a single FtsZ-GFP molecule.

We can rewrite Eqs. 1 and 2 at steady state as

$$\frac{d(Z_{t,ss}+\delta Z_t)}{dt} = -2k_E n_{p,ss}\delta Z_t - 2\left(k_E Z_{t,ss} + k_S - k_E Z_t\right)\delta n_p \tag{6}$$

$$\frac{d(n_{p,ss}+\delta n_p)}{dt} = k_B\delta Z_t - \left(2k_L n_{p,ss} + 3k_B\right)\delta n_p \tag{7}$$

where all the higher order terms have been omitted. In Eq. 6, replacing $Z_{r,ss}$ and $n_{p,ss}$ with the expression in Eq. 3 yields the solution

$$\delta Z_r(t) = \delta Z_r(0) e^{\frac{k_E\left(3k_B - \sqrt{9k_B^2 + 4k_L k_B\left(Z_t - k_S/k_E\right)}\right)}{k_L}t}. \tag{8}$$

Therefore, the autocorrelation function (Eq. 7) can be written as a single exponential

$$C_I(\tau) = Q^2\langle \delta Z_r(0)^2\rangle e^{k_{\mathrm{ex}}t} \tag{9}$$

where k_{ex} is the stochastic exchange rate of FtsZ subunits, and is a function of the rate constants k_E, k_S, k_B, and k_L.

The normalized PSD of this model can then be calculated from the normalized autocorrelation function using the Wiener-Khinchin theorem (*47*):

$$\mathrm{PSD}(\nu) = \int_{-\infty}^{\infty} \frac{C_I(\tau)}{Q^2\langle \delta Z_r(0)^2\rangle} e^{-2\pi i f\tau} d\tau = 2\frac{k_{\mathrm{ex}}}{(2\pi f)^2 + {k_{\mathrm{ex}}}^2}. \tag{10}$$

Supplemental Figures

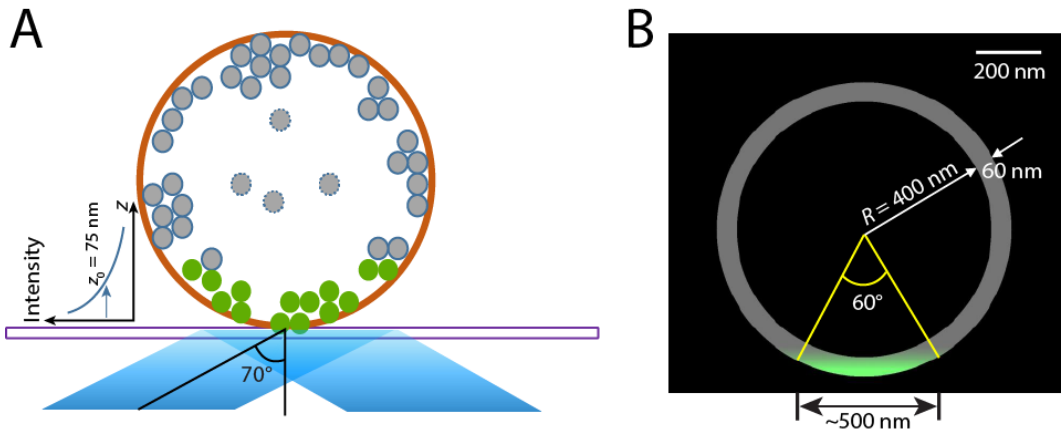

Figure S1: TIRF illumination geometry. (A) The TIRF angle was set to 70°, which gives a characteristic excitation depth of ~75-80 nm along the *z*-axis for 488-nm illumination. (B) The calculated GFP excitation field (green shading), considering the TIRF illumination depth, the radius of the cell (~500 nm), and Z-ring dimensions (~400 nm from the cell center with a 60-nm radial thickness), has a width of ~500 nm at the bottom of the cell. This 500 nm-wide region corresponds to approximately 1/6 of the Z-ring and was cropped out from time-lapse movies for data analysis.

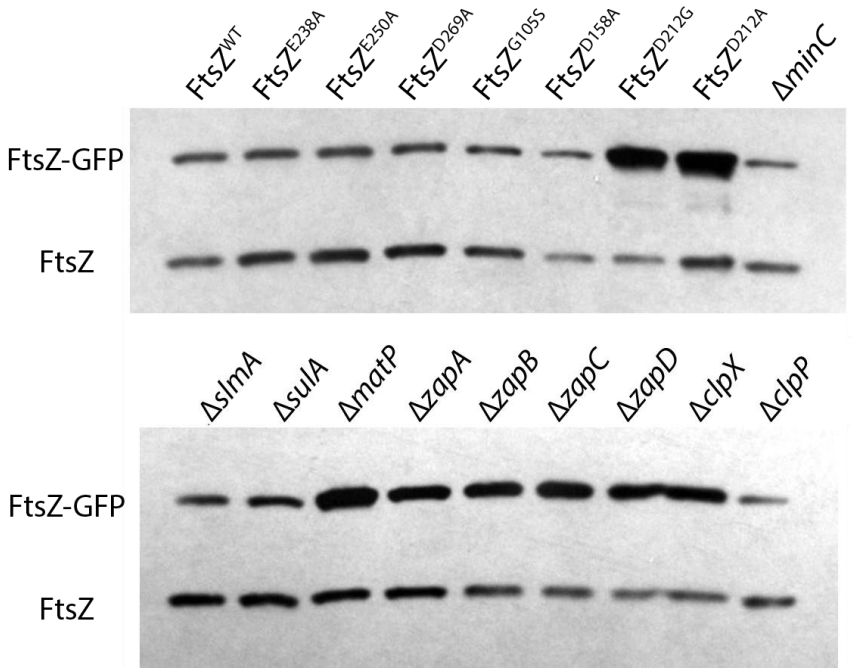

Figure S2: A representative immunoblot of FtsZ and FtsZ-GFP (WT and mutants). FtsZ-GFP was expressed under the same experimental conditions as for imaging, and blotted using an anti-FtsZ antibody.

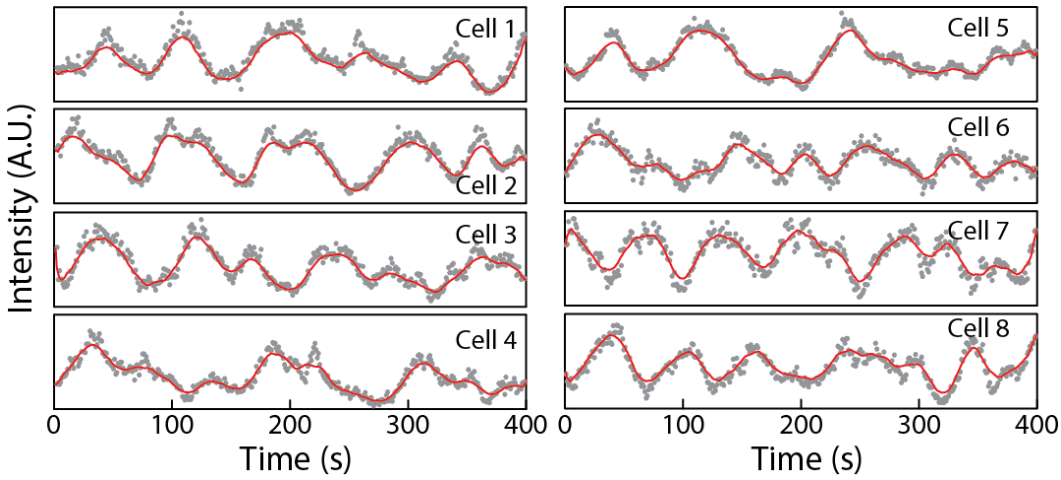

Figure S3: Additional representative fluorescence time traces of FtsZ-GFP in the TIRF region of assembled Z-rings similar to Fig. 1B.

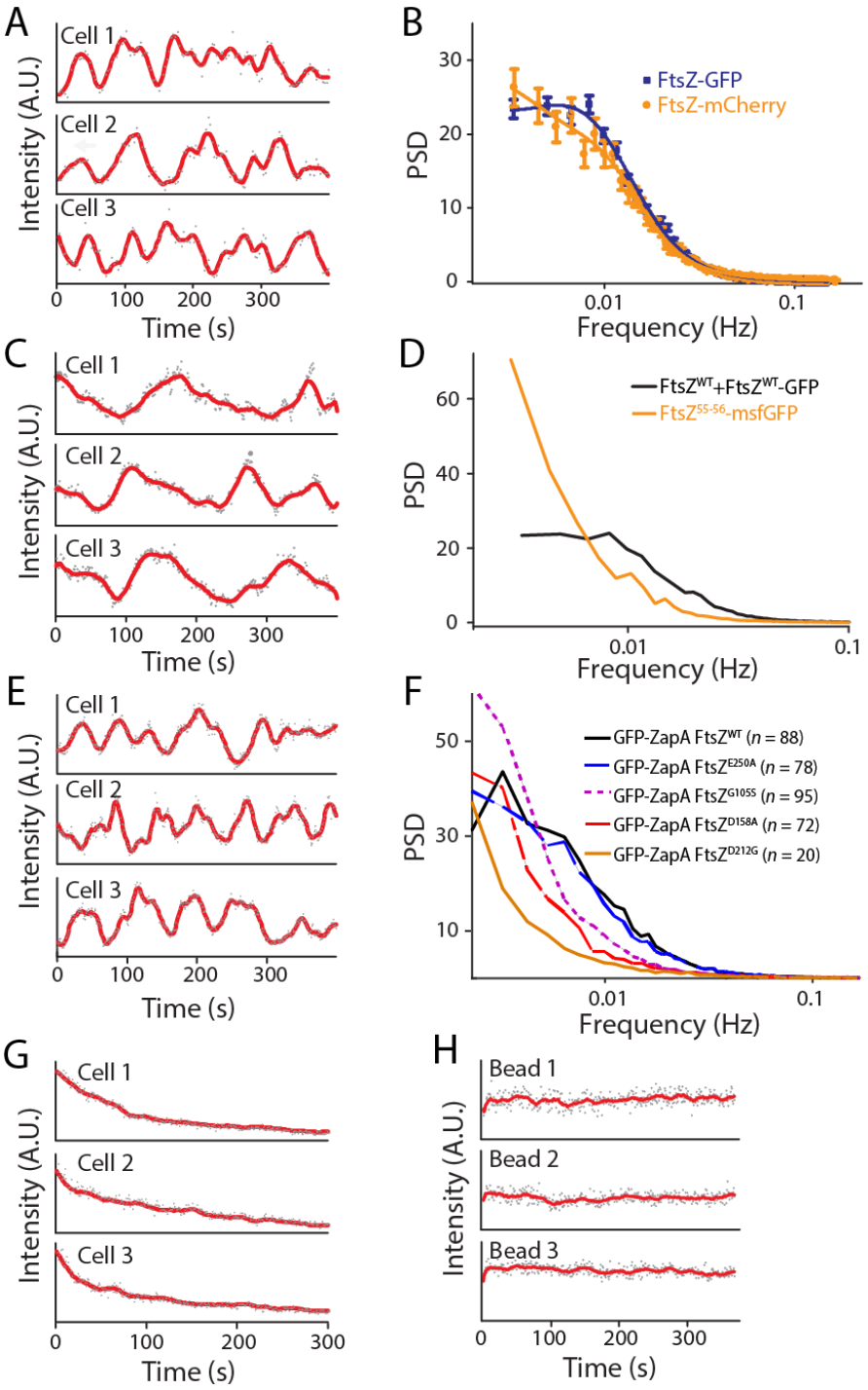

Figure S4: Representative fluorescence intensity time traces (twenty points moving-averaged) using FtsZ-mCherry (A), FtsZ$^{55\text{-}56}$-msfGFP (C), GFP-ZapA (E) in live cells, FtsZ-GFP in fixed cells (G), and immobilized fluorescence beads (H). (B) Comparison of the PSD curve of FtsZ-mCherry with FtsZ-GFP. The fitted values of k_{ex} (0.056 ± 0.008 s^{-1}) and the periodic frequency (0.008 ± 0.001 Hz) are similar to those of FtsZ-GFP. (D) PSD curve of FtsZ$^{55\text{-}56}$-msfGFP indicates slower dynamic behavior compared with FtsZ^{WT} (see fig. S5 for more details). (F) PSD curves of GFP-ZapA in FtsZ GTPase mutant strains showed a similar trend as that of FtsZ-GFP (Fig. 1J).

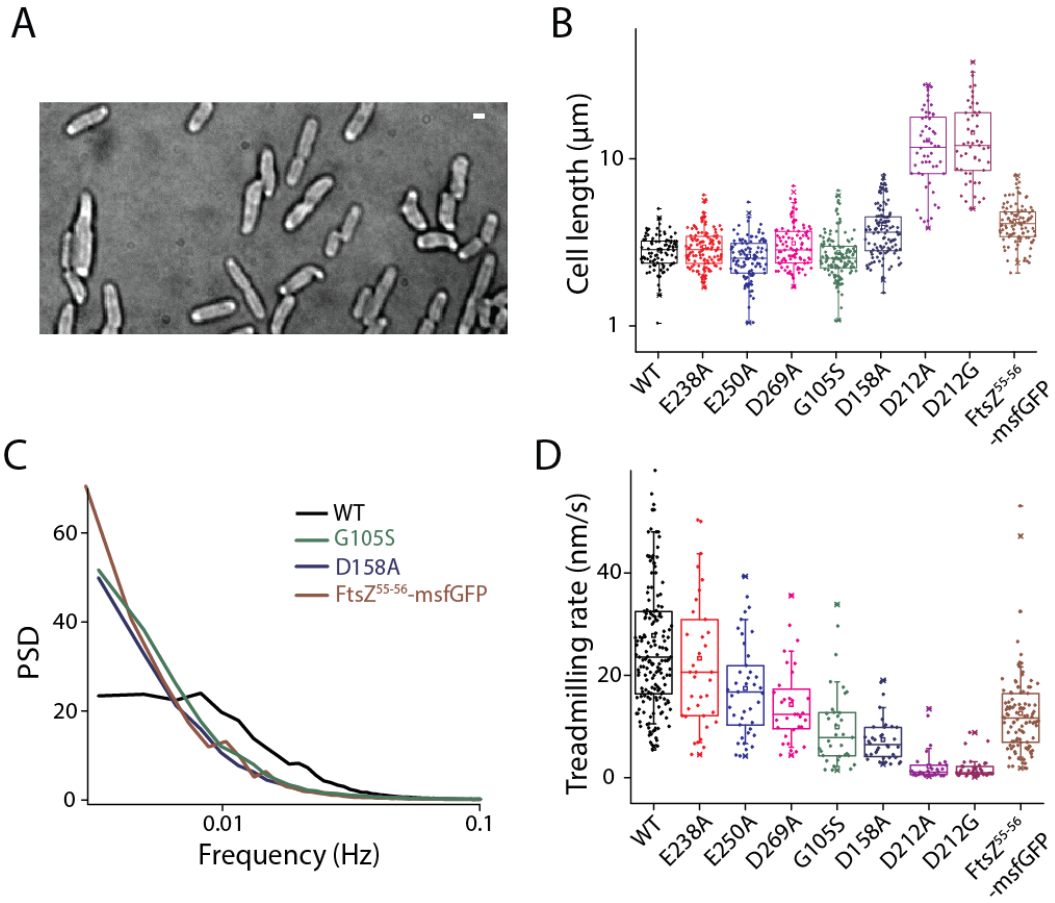

Figure S5: Comparison of FtsZ$^{55\text{-}56}$-msfGFP with FtsZ^{mut} strains. (A) Cells solely expressing FtsZ$^{55\text{-}56}$-msfGFP were longer and had irregular morphology than BW25113 cells. Scale bar: 1 μm. (B) The average length of FtsZ$^{55\text{-}56}$-msfGFP cells was 4.2 ± 1.2 μm (mean ± s.d.), significantly longer than WT and intermediate between the D158A and D212A mutants. (C) The average PSD curve of FtsZ$^{55\text{-}56}$-msfGFP was similar to the G105S and D158A mutants. (D) FtsZ$^{55\text{-}56}$-msfGFP treadmilling speed was ~2-fold lower than wild-type cell (12.6 ± 8.1 nm/s, mean ± s.d.), and between that of the D269A and G105S mutants. Many Z-rings in a similar strain (FtsZ$^{55\text{-}56}$-mNeonGreen) also showed helical structures (Movie S19).

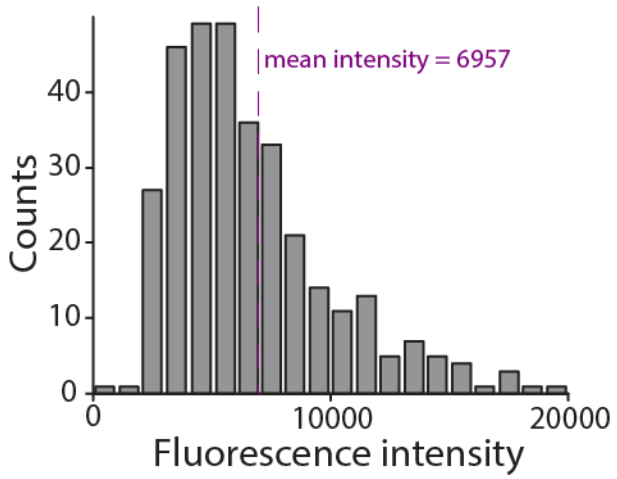

Figure S6: Distribution of total FtsZ-GFP fluorescence intensity in the TIRF imaging area of individual cells.

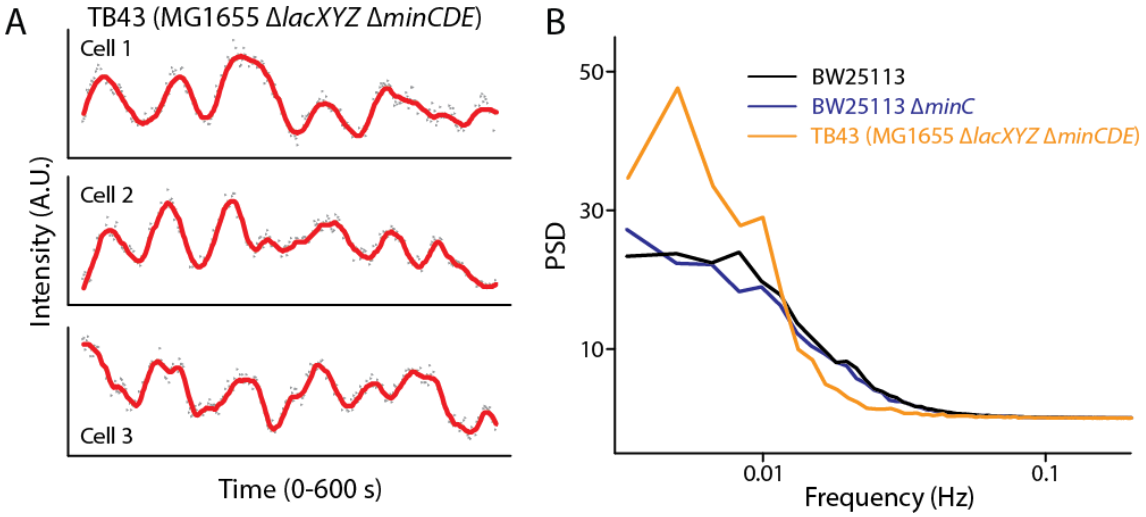

Figure S7: FtsZ dynamics in a strain lacking the *minCDE* operon. (A) Representative fluorescence intensity time traces (twenty points moving-averaged) showing periodic fluctuations. (B) Mean PSD curves were highly similar for BW25113 WT and Δ*minC*. The PSD curve for TB43 cells was qualitatively similar, with quantitative differences that may be due either to differences between Δ*minC* and Δ*minCDE,* or between the strain backgrounds (TB28 vs. BW25113).

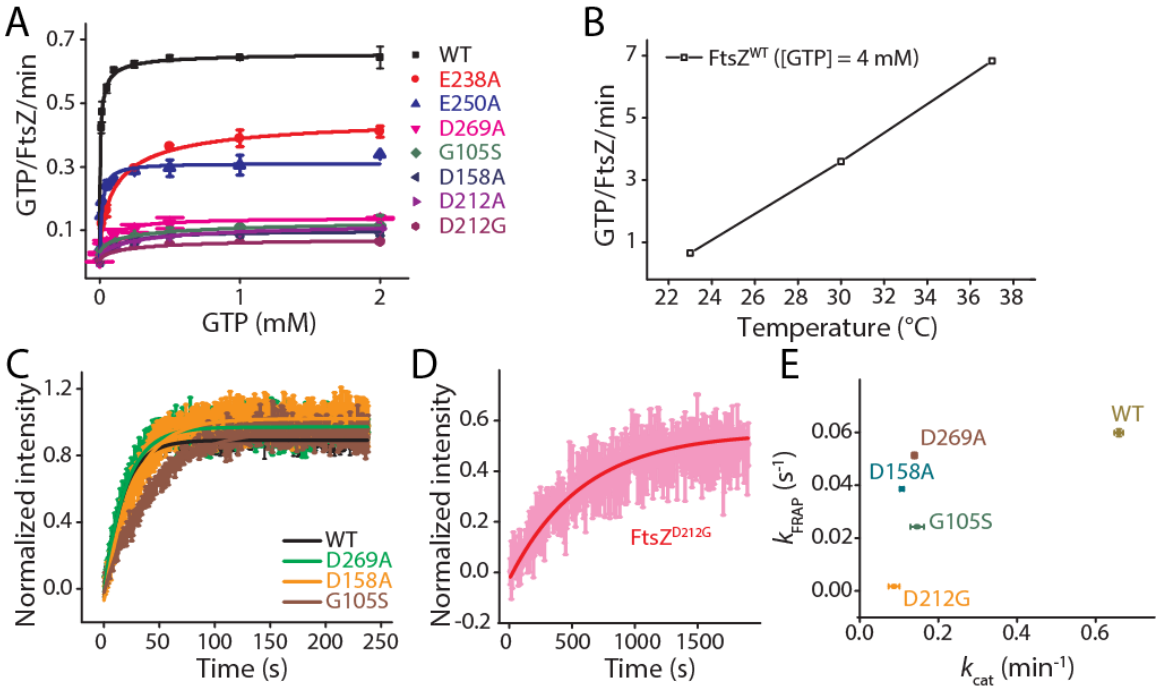

Figure S8: In vitro GTPase activity measurements and in vivo fluorescence recovery after photobleaching (FRAP) of FtsZ GTPase mutants. (A) Hill-modified Michaelis-Menten analysis (*18*) of GTP hydrolysis rates as a function of GTP concentration. The fitted values of k_{cat} and K_m are given in Table S1. Error bars are s.e.m., n = 3 independent experiments. (B) GTPase activity of the FtsZ^{WT} protein increased linearly with temperature, consistent with previous measurements at 30 °C or 37 °C. GTP concentration was 4 mM. (C, D) FRAP curves of FtsZ^{mut}-GFP. The curves were averaged over three experiments with (C) ~40 Z-rings in the WT, D269A, D158A, and G105S strains, and (D) ~20 Z-rings in the D212G strain. (E) Relationship between GTPase activity and FRAP rate constant. Error bars are standard deviation in (C-E).

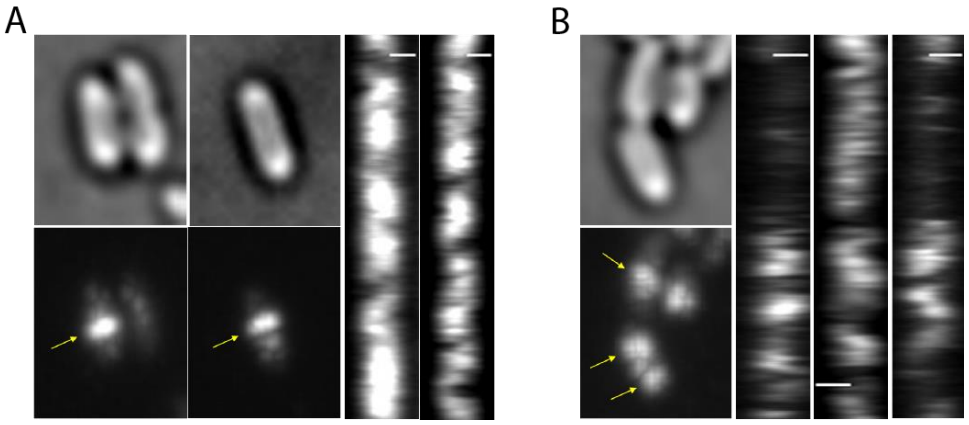

Figure S9: Additional representative kymographs of FtsZ-GFP showing zigzags that indicate directional movement of FtsZ polymers. (A) Cells with midcell Z-rings. (B) Cells with midcell-localized FtsZ but without clearly assembled Z-rings. Bright-field images and maximum intensity projections of each cell are shown on the left, with the corresponding kymographs at positions indicated by arrows in the maximum intensity projection shown on the right. The total time for each movie is 400 s (frame rate: 1 frame/s, scale bars: 0.5 μm). Corresponding time-lapse movies are in Movies S4 to S7.

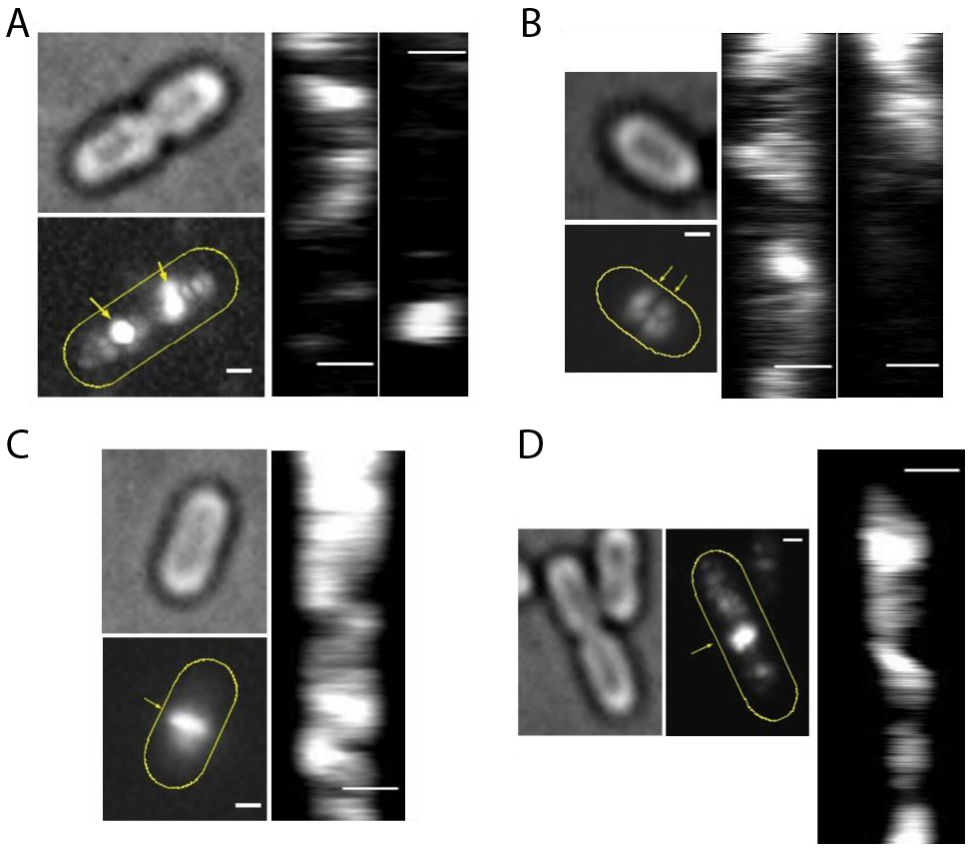

Figure S10: Additional representative kymographs of FtsZ polymers from TIRF imaging with higher spatial and temporal resolution. Zigzag motion was apparent predominantly in short cells (64% of cells with length < 2.8 μm, *n* = 53). (A-D) FtsZ dynamics at different points in the cell cycle: before midcell Z-ring assembly (A and B), after midcell Z-ring assembly (C), and in cells with deep constrictions (D). Bright-field images and maximum intensity projections of each cell are shown on the left, with the corresponding kymographs at positions indicated by arrows in the maximum intensity projection shown on the right. The total time for each movie is 200 s (frame rate: 2 frames/s, scale bars: 0.5 μm). Corresponding time-lapse movies are in Movies S10 to S13.

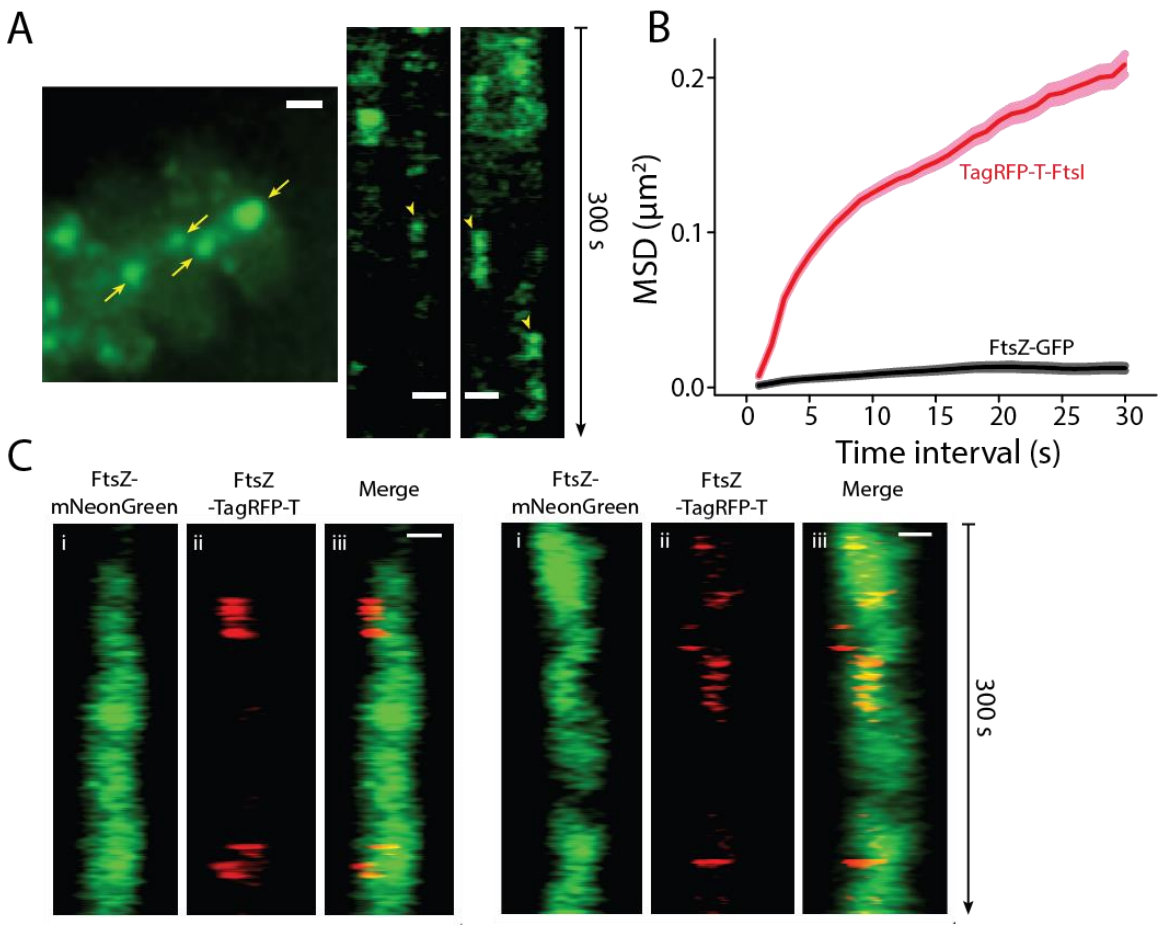

Figure S11: FtsZ single-molecule dynamics. (A) Tracking of single FtsZ-GFP molecules with long exposures. The maximum intensity projection (left) indicates that most FtsZ localize to mid-cell (yellow arrows). The corresponding kymographs (right) show short-lived FtsZ molecules confined at certain places without directional movement (arrowheads). (B) The mean squared displacement of FtsZ molecules showed significantly slower mobility comparing to FtsI (both septal and non-septal located), confined to a ~100nm region that is smaller than the typical treadmilling distance (~750 nm) over a 30-s interval. Number of trajectories > 3000. (C) Kymographs of single FtsZ-TagRFP-T molecules (ii) along with Z-ring dynamics in $FtsZ^{55-56}$-mNeonGreen cells (i). The merged kymographs (iii) showed no direct correlation between single FtsZ movement and Z-ring treadmilling behavior. Scale bars: 0.5 μm.

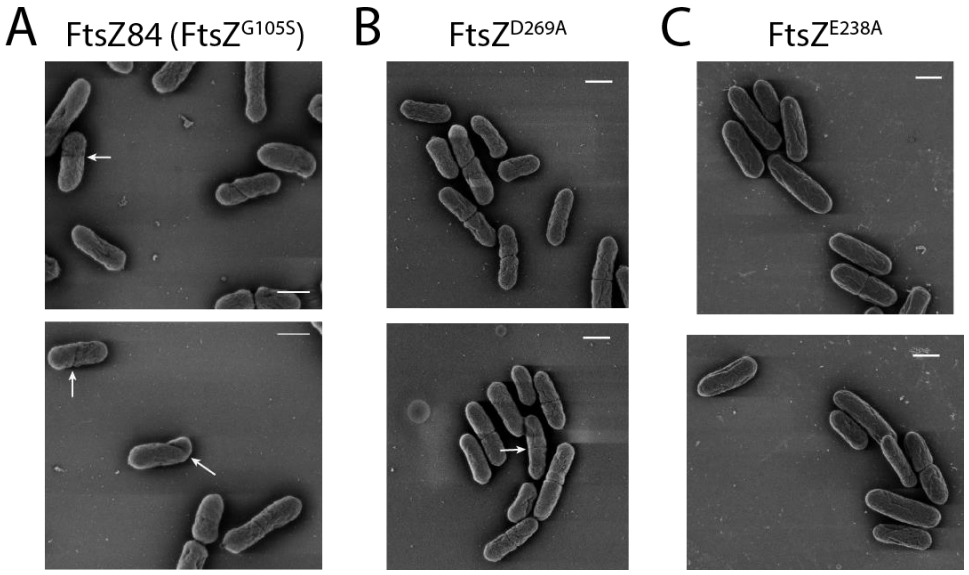

Figure S12: Additional SEM images of FtsZ mutant strains. (A) FtsZ84 (FtsZ^{G105S}), (B) FtsZ^{D269A}, and (C) FtsZ^{E238A}. Arrows denote incomplete septa. Scale bars: 1 μm.

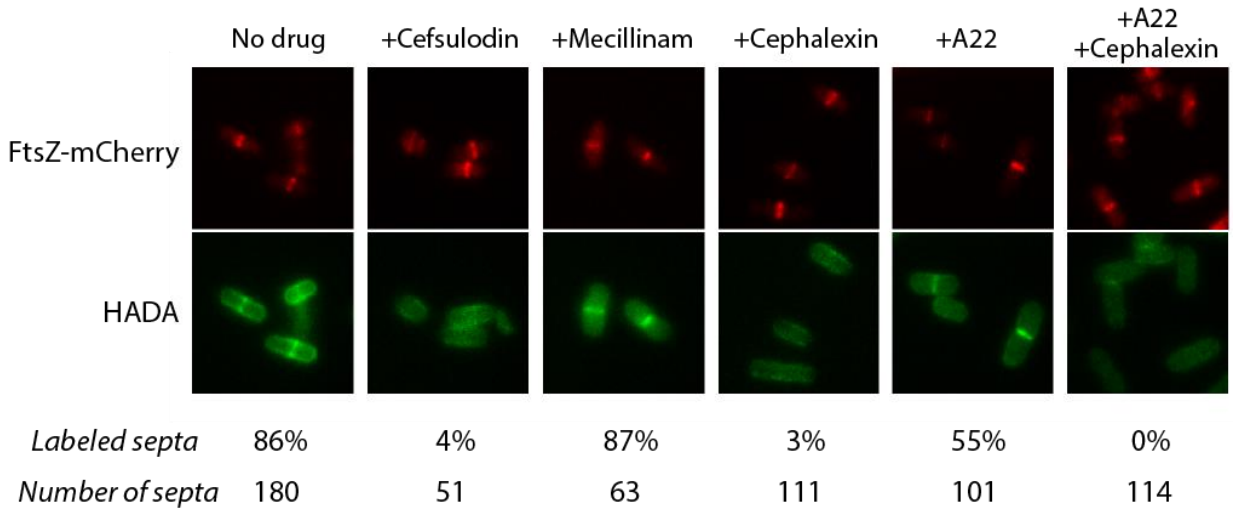

Labeled septa	86%	4%	87%	3%	55%	0%
Number of septa	180	51	63	111	101	114

Figure S13: HADA incorporation in drug-treated cells. The total number of septa was calculated by counting the number of cells with midcell Z-rings as indicated by FtsZ-mCherry fluorescence, of which the number of HADA-labeled septa was counted. Blocking PBP1b (cefsulodin), FtsI (cephalexin), or MreB+FtsI (A22+cephalexin) abolished HADA incorporation, while blocking PBP2 (mecillinam) alone had no effect, and blocking MreB (A22) decreased HADA incorporation in half of the cells.

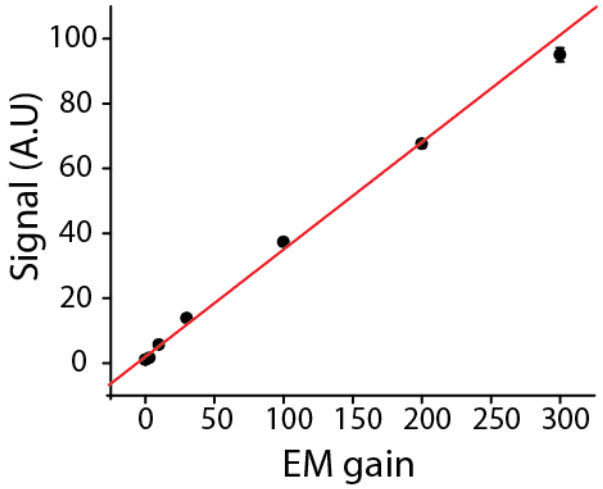

Figure S14: Calibration of camera electron multiplier (EM) gain using fluorescent beads. Normalized signal intensity from fluorescent beads increased linearly with EM gain.

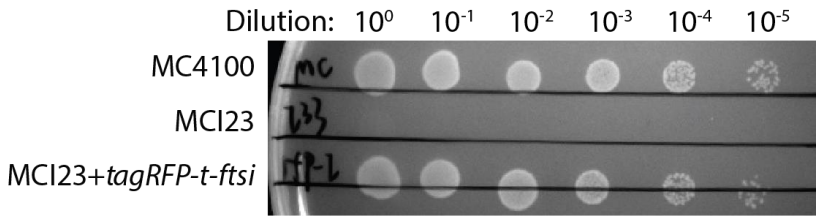

Figure S15: Spot-dilution assay illustrating complementation by TagRFP-T-FtsI in the FtsI temperature-sensitive strain MC123. The plate was incubated on LB plates at 42 °C overnight. MC4100 was spotted in the same way as a WT control.

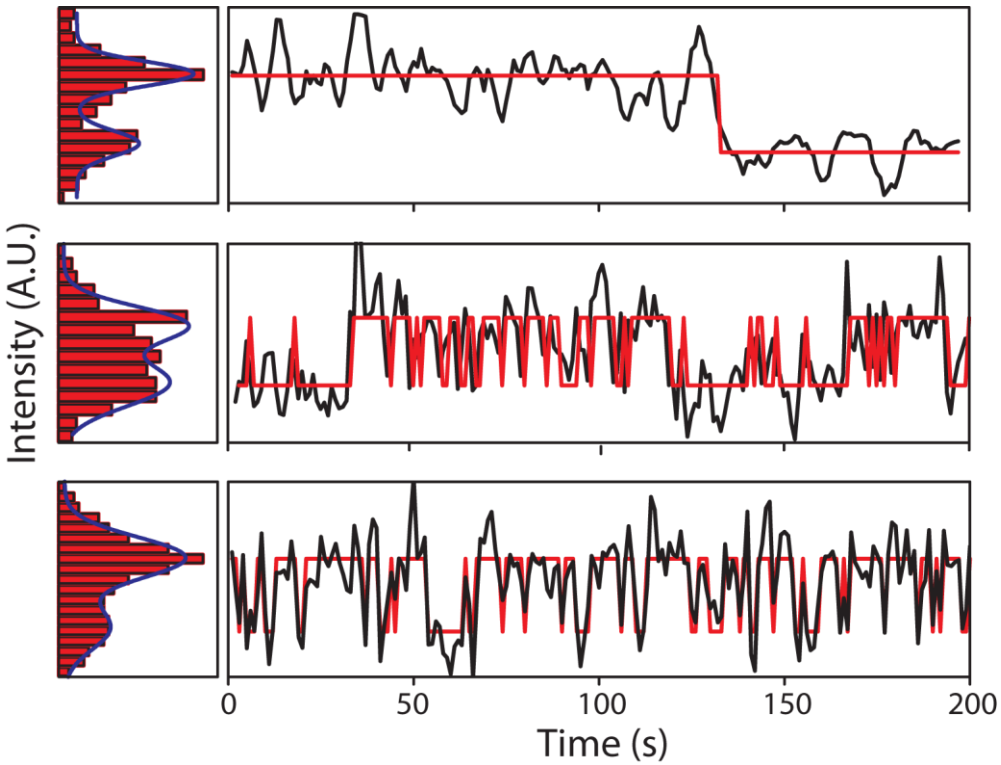

Figure S16: Representative single-molecule fluorescence intensity traces of TagRFP-T-FtsI. Time traces (black curves) exhibited characteristic single-molecule two-state blinking and/or abrupt bleaching events (fitted red stepwise functions). The corresponding florescence intensity also exhibited typical two-state distributions, as shown on the left.

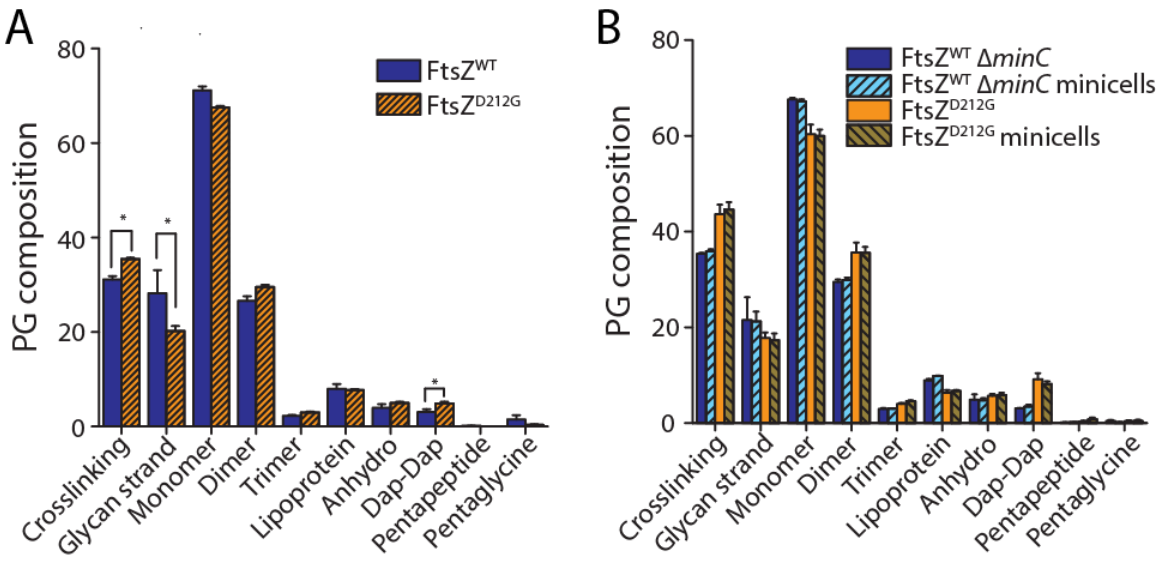

Figure S17: Comparison of PG composition in FtsZ WT and D212G cells. (A) Cells grown in LB showed increased crosslinking and shorter glycan strands, as in M9 (Fig. 4F). (B) Minicells harvested from BW25113 Δ*minC* or BW25113 FtsZ^{D212G} cultures had the same PG composition as whole cells.

Supplementary Tables

Table S1: In vitro and in vivo measurements of FtsZ WT and mutant protein dynamics.

FtsZ variant	k_{cat} (min^{-1})	K_m (μM)	k_{ex} (s^{-1})	k_{FRAP} (s^{-1})	Frequency (Hz)	Polymerization rate (nm/s)	Depolymerization rate (nm/s)	FtsZ treadmilling speed (nm/s)	FtsI speed (nm/s)
WT	0.66±0.01[a]	4.8±1.6[a]	0.051±0.003[b]	0.060±0.001[c]	0.0087±0.0007[d]	30.0±17.3[e]	-25.5±16.6[e]	27.8±17.1[f]	19.3±21.2[g]
E238A	0.46±0.03	109±26	0.060±0.002	ND	0.0103±0.0009	24.6±15.2	-22.0±14.0	23.3±14.9	ND
E250A	0.31±0.01	15±2	0.039±0.002	ND	0.0116±0.0012	18.1±10.6	-16.7±7.1	17.4±9.2	13.5±13.3
D269A	0.14±0.01	64±10	0.031±0.002	0.051±0.001	0.0850±0.001	14.8±6.4	-13.8±8.3	14.3±7.5	ND
G105S	0.15±0.02	153±64	0.021±0.003	0.024±0.001	0.0047±0.0003	10.7±8.7	-9.1±6.3	9.9±7.8	ND
D158A	0.107±0.005	138±19	0.019±0.002	0.039±0.001	0.0034±0.0004	7.9±4.8	-6.8±3.6	7.4±4.2	8.0±6.6
D212A	0.135±0.005	249±35	0.0077±0.0006	ND	0.0019±0.0002	2.1±2.8	-2.6±3.6	2.3±3.2	ND
D212G	0.09±0.01	239±137	0.0050±0.0001	0.0017±0.0001	0.0020±0.0003	1.7±1.7	-1.9±2.3	1.8±2.3	4.9±5.0

a. The error is standard error of the mean (s.e.m.), with $n = 3$.
b. The error is standard deviation (s.d.) of fitting.
c. The error is s.d., with $n > 20$.
d. The error is the bootstrapped ($n > 1000$) s.d. of the peak frequency.
e. The error is s.e.m. with $n > 40$.
f. The error is s.e.m. with $n > 40$.
g. The error is s.e.m. with $n > 30$.

Table S2: In vivo measurements of FtsZ periodic dynamics in drug-treated cells.

Drug (200 μg/mL)	k_{ex} (s^{-1})	Frequency (Hz)
A22	0.042±0.002[a]	0.0093±0.0011[b]
Mecillinam	0.044±0.002	0.0107±0.0014
Cefsulodin	0.042±0.002	0.0085±0.0002
Cephalexin	0.047±0.004	0.0094±0.0003

a. The error is the standard deviation (s.d.) of fitting.
b. The error is the bootstrapped (n > 1000) s.d. of the peak frequency.

Table S3: *In vivo* measurements of FtsZ periodic dynamics in strains lacking proteins that regulate or stabilize the Z-ring.

Genotype	k_{ex} (s^{-1})	Frequency (Hz)
Δ*minC*	0.039±0.001[a]	0.0106±0.0006[b]
Δ*slmA*	0.045±0.001	0.0113±0.0008
Δ*sulA*	0.048±0.002	0.0093±0.0005
Δ*matP*	0.040±0.002	0.0092±0.0008
Δ*zapA*	0.038±0.002	0.0086±0.0005
Δ*zapB*	0.032±0.002	0.0071±0.0012
Δ*zapC*	0.055±0.004	0.0108±0.0008
Δ*zapD*	0.047±0.003	0.0091±0.0006
Δ*clpX*	0.028±0.002	0.0091±0.0033
Δ*clpP*	0.030±0.001	0.0107±0.0031

a. The error is standard deviation (s.d.) of fitting.
b. The error is the bootstrapped (n > 1000) s.d. of the peak frequency.

Table S4: Single nucleotide variants in FtsZ mutant strains.

FtsZ variant	Position[a]	Mutation	Note	Position[a]	Mutation	Note
E238A	2855198	C→ CGCACTAG	Intergenic region	2746270	T→C	IRU repeat sequence
E250A	2855198	C→ CGCACTAG	Intergenic region			
D269A	2855198	C→ CGCACTAG	Intergenic region			
G105S	2855198	C→ CGCACTAG	Intergenic region			
D158A	2855198	C→ CGCACTAG	Intergenic region			
D212A	2855198	C→ CGCACTAG	Intergenic region			
D212G	2855198	C→ CGCACTAG	Intergenic region			

a. The position refers to the *E. coli* K12 strain DH10B genome.

Table S5: Cell Length, constriction rate (v_c), and elongation rate during division (v_{ec}) of FtsZ mutant strains.

FtsZ variant	Cell length (μm)	v_c (nm/min)	v_{ec} (nm/min)	v_c/v_{ec}
WT	2.8±0.6[a] (*n*=102)	14.8±0.6[b]	12.3±0.5[b] (*n*=48)	1.20±0.07[c]
E238A	2.9±0.8 (*n* =129)	12.2±0.5	10.6±0.7 (*n*=41)	1.15±0.09
E250A	2.6±0.7 (*n* =113)	13.2±0.4	11.6±0.0.7 (*n*=40)	1.14±0.05
D269A	3.1±1.0 (*n* =100)	ND	ND	ND
G105S	2.7±0.9 (*n*=137)	14.5±0.4	11.4±0.5 (*n*=46)	1.27±0.07
D158A	3.8±1.4 (*n*=117)	14.2±0.5	13.4±1.0 (*n*=42)	1.06±0.09
D212A	12.7±6.3 (*n*=54)	ND	ND	ND
D212G	14.1±7.6 (*n*=51)	ND	ND	ND

a. Cell length was measured from bright-field images taken under the same conditions as FtsZ dynamics measurements. The error is the standard deviation (s.d.).
b. The error is calculated from the standard error of the mean (s.e.m.) of the diameter/length and the time.
c. The error is calculated from that of v_c and v_{ec}.

Table S6. Strains, plasmids, and primers used in this study.

Strain	Genotype	Reference/source
BW25113	F-, Δ*(araD-araB)567*, Δ*lacZ4787(::rrnB-3)*, *rph-1*, Δ*(rhaD-rhaB)568*, *hsdR514*	CGSC #8590 (*38*)
XY058	BW25113 *ftsZG105S(ts)*	This study
XY072	BW25113 *ftsZE250A*	This study
XY075	BW25113 *ftsZD158A*	This study
XY076	BW25113 *ftsZD212G(ts)*	This study
XY088	BW25113 *ftsZE238A*	This study
XY089	BW25113 *ftsZD269A*	This study
XY129	BW25113 *ftsZD212A(ts)*	This study
JW1165	BW25113 Δ*minC*::*kan*	CGSC #9075 (*48*)
JW5641	BW25113 Δ*slmA*::*kan*	CGSC #11495 (*48*)
JW0941	BW25113 Δ*sulA*::*kan*	CGSC #8943 (*48*)
JW2878	BW25113 Δ*zapA*::*kan*	CGSC #10232 (*48*)
JW3899	BW25113 Δ*zapB*::*kan*	CGSC #10814 (*48*)
JW5125	BW25113 Δ*zapC*::*kan*	CGSC #12062 (*48*)
JW0099	BW25113 Δ*zapD*::*kan*	CGSC #8381 (*48*)
JW0428	BW25113 Δ*clpX*::*kan*	CGSC #8591 (*48*)
JW0427	BW25113 Δ*clpP*::*kan*	CGSC #8590 (*48*)
JW0939	BW25113 Δ*matP*::*kan*	CGSC #12061 (*48*)
MCI23	MC4100 *ftsI23*(*ts*) *leu-260*::*Tn10*	CGSC #12061 (*48*)
KC606	BW25113 *ftsZ*::*ftsZ*$^{55\text{-}56}$*-sfGFP*	This study
XY106	BW25113 P_{BAD}::*ftsZ-GFP*	This study
XY263	BW27783 *ftsZ*::*ftsZ*$^{55\text{-}56}$*-mNeonGreen*, P_{lac}::*ftsZ-tagRFP-t*	This study
TB43	Δ*lacIZYA*::*frt* Δ*minCDE*::*frt*	(*49*)
Plasmid	**Genotype**	**Reference/source**
JW0093	ColEI, $P_{T5\text{-}lac}$::*6xHis-ftsZ-gfp cat*	(*50*)
pXY021	ColEI, $P_{T5\text{-}lac}$::*6xHis-ftsZG105S-gfp cat*	(*11*)
pXY036	ColEI, $P_{T5\text{-}lac}$::*6xHis-ftsZE250A-gfp cat*	This study
pXY035	ColEI, $P_{T5\text{-}lac}$::*6xHis-ftsZE238A-gfp cat*	This study
pXY033	ColEI, $P_{T5\text{-}lac}$::*6xHis-ftsZD158A-gfp cat*	This study
pXY092	ColEI, $P_{T5\text{-}lac}$::*6xHis-ftsZD269A-gfp cat*	This study
pXY054	ColEI, $P_{T5\text{-}lac}$::*6xHis-ftsZD212A-gfp cat*	This study
pXY040	ColEI, $P_{T5\text{-}lac}$::*6xHis-ftsZD212G-gfp cat*	This study
pXY018	ColEI, $P_{T5\text{-}lac}$::*gfp-zapA cat*	This study
pXY104	pSC101, P_{BAD}::*ftsZ-GFP specR*	This Study
pRM006	ColEI, P_{T7}::*His-sumo-ftsZ amp*	This study
pXY142	ColEI, P_{T7}::*His-sumo-ftsZG105S amp*	This study
pXY196	ColEI, P_{T7}::*His-sumo-ftsZE250A amp*	This study
pXY197	ColEI, P_{T7}::*His-sumo-ftsZE238A amp*	This study
pXY194	ColEI, P_{T7}::*His-sumo-ftsZD158A amp*	This study
pXY195	ColEI, P_{T7}::*His-sumo-ftsZD269A amp*	This study
pXY148	ColEI, P_{T7}::*His-sumo-ftsZD212G amp*	This study
pXY198	ColEI, P_{T7}::*His-sumo-ftsZD212A amp*	This study
pJB007	ColEI, $P_{T5\text{-}lac}$::*TagRFP-t-ftsI cat*	This study
pTB146	ColEI, P_{T7}::*His-sumo amp*	From E. Goley
pCH033	ColEI, $P_{T5\text{-}lac}$::*ftsZ-tagRFP-t-ftsI cat*	(*11*)
Primers	**Sequence (5'→3')**	**Note**
1	GGGTATGAGTGGTGGTACCGGTACAGGTGC	FtsZ site-directed mutagenesis WT→G105S
2	CACCACTCATACCCGCAGCAATAAAGACCATGTC	
3	CTGTCCAAGCATGTGGCCTCTCTGATCACTATCC	FtsZ site-directed mutagenesis WT→D158A
4	GGATAGTGATCAGAGAGGCCACATGCTTGGACAG	
5	GAACGTGGACTTTGCAGGCGTACGCACCGTAATG	FtsZ site-directed mutagenesis WT→D212G
6	CATTACGGTGCGTACGCCTGCAAAGTCCACGTTC	
7	GAACGTGGACTTTGCAGCCGTACGCACCGTAATG	FtsZ site-directed mutagenesis WT→D212A
8	CATTACGGTGCGTACGGCTGCAAAGTCCACGTTC	
9	GAAGACCGTGCGGAAGCAGCTGCTGAAATGGC	FtsZ site-directed mutagenesis WT→E238A
10	GCCATTTCAGCAGCTGCTTCCGCACGGTCTTC	
11	CTTCTCCGCTGCTGGCAGATATCGACCTGTC	FtsZ site-directed mutagenesis WT→E250A
12	GACAGGTCGATATCTGCCAGCAGCGGAGAAG	
13	ATCACGGCGGGCTTCGCTCTGCGTCTGGATGA	FtsZ site-directed mutagenesis WT→D269A
14	TCATCCAGACGCAGAGCGAAGCCCGCCGTGAT	
15	GAGCTCTTCTGGTATGTTTGAACCAATGGAACTTAC	*ftsZ* gene amplification
16	GTGCGGCCGCTTAATCAG	

17	GAACCAATGGAACTTACCAATGACGC	*ftsZ-frt-kan-frt* fragment amplification
18	gtataggaacttcgaagcagTTAATCAGCTTGCTTACGCAGGAATG	
19	CATTCCTGCGTAAGCAAGCTGATTAActgcttcgaagttcctatac	
20	GTTTAGCACAAAGAGCCTCGAAACCCAAATTCCAGTCAATTCgcagttcgaagttcctattc	
21	GTTTAGCACAAAGAGCCTCGAAACC	
22	GCATCAGTTGGCTCGTGGATCAAG	*fts*Z gene amplification from the chromosomal locus
23	GTAACGTCAGGGTGACTTTCTTGC	
24	CTTAACTAGTATGGTGTCTAAGGGCGAAGAGCTGATTA	*tagRFP-t* amplification
25	CTATGAATTCGCCAGAACCAGCAGCGGAGCCAGCGGATCCCTTGTACAGCTCGTCCATG CCA	
26	CTTAGAATTCATGAAAGCAGCGGCGAAAAC	*ftsI* amplification
27	CTATGTCGACTTACGATCTGCCACCTGTCC	
28	CAGCTGCGCTAGCATGTTTGAACCAATGGAACTTACCAATG	*ftsZ-gfp* amplification
29	CTGTCTGCAGGTCGACTTATTTGTATAGTTCATCCATGCCATGTG	

Supplemental Movie Legends

Movie S1

TIRF time-lapse movie of FtsZ-GFP fluorescence fluctuations in the cell shown in Fig. 1A. Frame rate = 1 frame/s; camera pixel size = 167 nm. The cell is outlined in yellow with the arrow pointing at the Z-ring at midcell. Scale bar: 0.5 μm.

Movie S2

An additional example TIRF time-lapse movie of FtsZ-GFP fluorescence fluctuations. Frame rate = 1 frame/s; camera pixel size = 167 nm. The cell is outlined in yellow with the arrow pointing at the Z-ring at midcell. Scale bar: 0.5 μm.

Movie S3

TIRF time-lapse movie of endogenously expressed $FtsZ^{55\text{-}56}$-msfGFP fluorescence fluctuations. Frame rate = 1.1 frames/s; camera pixel size = 100 nm. Scale bar: 1 μm.

Movie S4 to S7

TIRF time-lapse movies of FtsZ-GFP fluorescence fluctuations in the four cells in fig. S8 in which treadmilling behaviors were visible. Frame rate = 1 frame/s; camera pixel size = 167 nm. Cells are outlined in yellow with arrows pointing at the Z-rings at midcell. Scale bar: 0.5 μm.

Movie S8 to S13

TIRF time-lapse movies of FtsZ-GFP fluorescence with higher temporal (2 frames/s) and spatial (100 nm/pixel) resolution showed clear treadmilling of FtsZ polymers. Movies S7 and S8 correspond to the two cells shown in Fig. 2A and 2B. Movies S9 to S12 correspond to the four cells shown in fig. S9. Scale bar: 0.5 μm.

Movie S14

2D projection of 3D-SIM time-lapse movie of FtsZ-GFP. Frame rate = 6 frames/s; reconstructed pixel size = 30 nm. Arrows: titled or horizontal FtsZ rings with circumferential treadmilling. Scale bar: 1 μm.

Movie S15

Time-lapse movie of $FtsZ^{D212G}$ cells. Frame rate = 0.2 frames/min. The green channel is $FtsZ^{D212G}$-GFP, showing many twisted or helical rings. The arrows highlight the start and the completion of cell division. FtsZ was retained at the pole representing the last division site for a long interval even after the cells separated. Scale bar: 1 μm.

Movie S16 to S18

Epi-fluorescence time-lapse imaging of single TagRFP-T-FtsI molecules, showing directional movement along the septum. Frame rate = 1 frames/s; camera pixel size = 100 nm. Movies S13 to S16 correspond to the four $FtsZ^{WT}$ cells shown in Fig. 4A. Scale bar: 0.5 μm.

Movie S19

3D super-resolution reconstruction of a typical Z-ring in BW28773 *ftsZ*::*ftsZ*$^{55\text{-}56}$*-mNeonGreen* showing a spiral structure. Scale bar: 0.5 μm.

References

1. E. Nogales, K. H. Downing, L. A. Amos, J. Löwe, Tubulin and FtsZ form a distinct family of GTPases. *Nat. Struct. Biol.* **5**, 451–458 (1998). doi:10.1038/nsb0698-451 Medline

2. S. Vaughan, B. Wickstead, K. Gull, S. G. Addinall, Molecular evolution of FtsZ protein sequences encoded within the genomes of archaea, bacteria, and eukaryota. *J. Mol. Evol.* **58**, 19–29 (2004). doi:10.1007/s00239-003-2523-5 Medline

3. E. F. Bi, J. Lutkenhaus, FtsZ ring structure associated with division in *Escherichia coli*. *Nature* **354**, 161–164 (1991). doi:10.1038/354161a0 Medline

4. A. J. Egan, W. Vollmer, The physiology of bacterial cell division. *Ann. N.Y. Acad. Sci.* **1277**, 8–28 (2013). doi:10.1111/j.1749-6632.2012.06818.x Medline

5. P. de Boer, R. Crossley, L. Rothfield, The essential bacterial cell-division protein FtsZ is a GTPase. *Nature* **359**, 254–256 (1992). doi:10.1038/359254a0 Medline

6. D. Raychaudhuri, J. T. Park, *Escherichia coli* cell-division gene ftsZ encodes a novel GTP-binding protein. *Nature* **359**, 251–254 (1992). doi:10.1038/359251a0 Medline

7. Y. Chen, K. Bjornson, S. D. Redick, H. P. Erickson, A rapid fluorescence assay for FtsZ assembly indicates cooperative assembly with a dimer nucleus. *Biophys. J.* **88**, 505–514 (2005). doi:10.1529/biophysj.104.044149 Medline

8. J. Stricker, P. Maddox, E. D. Salmon, H. P. Erickson, Rapid assembly dynamics of the *Escherichia coli* FtsZ-ring demonstrated by fluorescence recovery after photobleaching. *Proc. Natl. Acad. Sci. U.S.A.* **99**, 3171–3175 (2002). doi:10.1073/pnas.052595099 Medline

9. H. P. Erickson, Modeling the physics of FtsZ assembly and force generation. *Proc. Natl. Acad. Sci. U.S.A.* **106**, 9238–9243 (2009). doi:10.1073/pnas.0902258106 Medline

10. E. Bi, J. Lutkenhaus, Analysis of ftsZ mutations that confer resistance to the cell division inhibitor SulA (SfiA). *J. Bacteriol.* **172**, 5602–5609 (1990). doi:10.1128/jb.172.10.5602-5609.1990 Medline

11. C. Coltharp, J. Buss, T. M. Plumer, J. Xiao, Defining the rate-limiting processes of bacterial cytokinesis. *Proc. Natl. Acad. Sci. U.S.A.* **113**, E1044–E1053 (2016). doi:10.1073/pnas.1514296113 Medline

12. See supplementary materials.

13. J. Buss, C. Coltharp, G. Shtengel, X. Yang, H. Hess, J. Xiao, A multi-layered protein network stabilizes the *Escherichia coli* FtsZ-ring and modulates constriction dynamics. *PLOS Genet.* **11**, e1005128 (2015). doi:10.1371/journal.pgen.1005128 Medline

14. D. A. Moore, Z. N. Whatley, C. P. Joshi, M. Osawa, H. P. Erickson, Probing for binding regions of the FtsZ protein surface through site-directed insertions: Discovery of fully

functional FtsZ-fluorescent proteins. *J. Bacteriol.* **199**, e00553-16 (2016). doi:10.1128/JB.00553-16 Medline

15. J. Buss, C. Coltharp, T. Huang, C. Pohlmeyer, S. C. Wang, C. Hatem, J. Xiao, In vivo organization of the FtsZ-ring by ZapA and ZapB revealed by quantitative super-resolution microscopy. *Mol. Microbiol.* **89**, 1099–1120 (2013). doi:10.1111/mmi.12331 Medline

16. V. W. Rowlett, W. Margolin, 3D-SIM super-resolution of FtsZ and its membrane tethers in *Escherichia coli* cells. *Biophys. J.* **107**, L17–L20 (2014). doi:10.1016/j.bpj.2014.08.024 Medline

17. M. P. Strauss, A. T. Liew, L. Turnbull, C. B. Whitchurch, L. G. Monahan, E. J. Harry, 3D-SIM super resolution microscopy reveals a bead-like arrangement for FtsZ and the division machinery: Implications for triggering cytokinesis. *PLOS Biol.* **10**, e1001389 (2012). doi:10.1371/journal.pbio.1001389 Medline

18. H. A. Arjes, B. Lai, E. Emelue, A. Steinbach, P. A. Levin, Mutations in the bacterial cell division protein FtsZ highlight the role of GTP binding and longitudinal subunit interactions in assembly and function. *BMC Microbiol.* **15**, 209 (2015). doi:10.1186/s12866-015-0544-z Medline

19. C. Lu, J. Stricker, H. P. Erickson, Site-specific mutations of FtsZ—effects on GTPase and in vitro assembly. *BMC Microbiol.* **1**, 7 (2001). doi:10.1186/1471-2180-1-7 Medline

20. B. D. Bennett, E. H. Kimball, M. Gao, R. Osterhout, S. J. Van Dien, J. D. Rabinowitz, Absolute metabolite concentrations and implied enzyme active site occupancy in *Escherichia coli*. *Nat. Chem. Biol.* **5**, 593–599 (2009). doi:10.1038/nchembio.186 Medline

21. S. Thanedar, W. Margolin, FtsZ exhibits rapid movement and oscillation waves in helix-like patterns in *Escherichia coli*. *Curr. Biol.* **14**, 1167–1173 (2004). doi:10.1016/j.cub.2004.06.048 Medline

22. M. Loose, T. J. Mitchison, The bacterial cell division proteins FtsA and FtsZ self-organize into dynamic cytoskeletal patterns. *Nat. Cell Biol.* **16**, 38–46 (2014). doi:10.1038/ncb2885 Medline

23. L. Niu, J. Yu, Investigating intracellular dynamics of FtsZ cytoskeleton with photoactivation single-molecule tracking. *Biophys. J.* **95**, 2009–2016 (2008). doi:10.1529/biophysj.108.128751 Medline

24. S. G. Addinall, J. Lutkenhaus, FtsZ-spirals and -arcs determine the shape of the invaginating septa in some mutants of *Escherichia coli*. *Mol. Microbiol.* **22**, 231–237 (1996). doi:10.1046/j.1365-2958.1996.00100.x Medline

25. E. Bi, J. Lutkenhaus, Isolation and characterization of ftsZ alleles that affect septal morphology. *J. Bacteriol.* **174**, 5414–5423 (1992). doi:10.1128/jb.174.16.5414-5423.1992 Medline

26. J. Stricker, H. P. Erickson, In vivo characterization of *Escherichia coli* ftsZ mutants: Effects on Z-ring structure and function. *J. Bacteriol.* **185**, 4796–4805 (2003). doi:10.1128/JB.185.16.4796-4805.2003 Medline

27. G. Fu, T. Huang, J. Buss, C. Coltharp, Z. Hensel, J. Xiao, In vivo structure of the *E. coli* FtsZ-ring revealed by photoactivated localization microscopy (PALM). *PLOS ONE* **5**, e12680 (2010). doi:10.1371/journal.pone.0012680 Medline

28. S. J. Holden, T. Pengo, K. L. Meibom, C. Fernandez Fernandez, J. Collier, S. Manley, High throughput 3D super-resolution microscopy reveals *Caulobacter crescentus* in vivo Z-ring organization. *Proc. Natl. Acad. Sci. U.S.A.* **111**, 4566–4571 (2014). doi:10.1073/pnas.1313368111 Medline

29. M. Jacq, V. Adam, D. Bourgeois, C. Moriscot, A. M. Di Guilmi, T. Vernet, C. Morlot, Remodeling of the Z-ring nanostructure during the *Streptococcus pneumoniae* cell cycle revealed by photoactivated localization microscopy. *MBio* **6**, e01108-15 (2015). doi:10.1128/mBio.01108-15 Medline

30. Z. Lyu, C. Coltharp, X. Yang, J. Xiao, Influence of FtsZ GTPase activity and concentration on nanoscale Z-ring structure in vivo revealed by three-dimensional superresolution imaging. *Biopolymers* **105**, 725–734 (2016). doi:10.1002/bip.22895 Medline

31. Z. Li, M. J. Trimble, Y. V. Brun, G. J. Jensen, The structure of FtsZ filaments in vivo suggests a force-generating role in cell division. *EMBO J.* **26**, 4694–4708 (2007). doi:10.1038/sj.emboj.7601895 Medline

32. J. Lutkenhaus, S. Pichoff, S. Du, Bacterial cytokinesis: From Z ring to divisome. *Cytoskeleton* **69**, 778–790 (2012). doi:10.1002/cm.21054 Medline

33. E. Kuru, H. V. Hughes, P. J. Brown, E. Hall, S. Tekkam, F. Cava, M. A. de Pedro, Y. V. Brun, M. S. VanNieuwenhze, In situ probing of newly synthesized peptidoglycan in live bacteria with fluorescent D-amino acids. *Angew. Chem. Int. Ed.* **51**, 12519–12523 (2012). doi:10.1002/anie.201206749 Medline

34. K. Sundararajan, A. Miguel, S. M. Desmarais, E. L. Meier, K. Casey Huang, E. D. Goley, The bacterial tubulin FtsZ requires its intrinsically disordered linker to direct robust cell wall construction. *Nat. Commun.* **6**, 7281 (2015). doi:10.1038/ncomms8281 Medline

35. A. W. Bisson-Filho, Y.-P. Hsu, G. R. Squyres, E. Kuru, F. Wu, C. Jukes, Y. Sun, C. Dekker, S. Holden, M. S. VanNieuwenhze, Y. V. Brun, E. C. Garner, Treadmilling by FtsZ filaments drives peptidoglycan synthesis and bacterial cell division. *Science* **355**, 739 (2017). doi:10.1126/science.aak9973

36. A. R. Paredez, C. R. Somerville, D. W. Ehrhardt, Visualization of cellulose synthase demonstrates functional association with microtubules. *Science* **312**, 1491–1495 (2006). doi:10.1126/science.1126551 Medline

37. N. C. Shaner, M. Z. Lin, M. R. McKeown, P. A. Steinbach, K. L. Hazelwood, M. W. Davidson, R. Y. Tsien, Improving the photostability of bright monomeric orange and red fluorescent proteins. *Nat. Methods* **5**, 545–551 (2008). doi:10.1038/nmeth.1209 Medline

38. K. A. Datsenko, B. L. Wanner, One-step inactivation of chromosomal genes in *Escherichia coli* K-12 using PCR products. *Proc. Natl. Acad. Sci. U.S.A.* **97**, 6640–6645 (2000). doi:10.1073/pnas.120163297 Medline

39. X. Wang, J. Huang, A. Mukherjee, C. Cao, J. Lutkenhaus, Analysis of the interaction of FtsZ with itself, GTP, and FtsA. *J. Bacteriol.* **179**, 5551–5559 (1997). doi:10.1128/jb.179.17.5551-5559.1997 Medline

40. S. Huecas, C. Schaffner-Barbero, W. García, H. Yébenes, J. M. Palacios, J. F. Díaz, M. Menéndez, J. M. Andreu, The interactions of cell division protein FtsZ with guanine nucleotides. *J. Biol. Chem.* **282**, 37515–37528 (2007). doi:10.1074/jbc.M706399200 Medline

41. K. Dai, Y. Xu, J. Lutkenhaus, Cloning and characterization of ftsN, an essential cell division gene in *Escherichia coli* isolated as a multicopy suppressor of ftsA12(Ts). *J. Bacteriol.* **175**, 3790–3797 (1993). doi:10.1128/jb.175.12.3790-3797.1993 Medline

42. A. Paintdakhi, B. Parry, M. Campos, I. Irnov, J. Elf, I. Surovtsev, C. Jacobs-Wagner, Oufti: An integrated software package for high-accuracy, high-throughput quantitative microscopy analysis. *Mol. Microbiol.* **99**, 767–777 (2016). doi:10.1111/mmi.13264 Medline

43. S. M. Desmarais, F. Cava, M. A. de Pedro, K. C. Huang, Isolation and preparation of bacterial cell walls for compositional analysis by ultra performance liquid chromatography. *J. Vis. Exp.* **2014**, e51183 (2014). doi:10.3791/51183 Medline

44. B. Glauner, Separation and quantification of muropeptides with high-performance liquid chromatography. *Anal Biochem.* **172**, 451–464 (1988). doi:10.1016/0003-2697(88)90468-X Medline

45. I. V. Surovtsev, J. J. Morgan, P. A. Lindahl, Kinetic modeling of the assembly, dynamic steady state, and contraction of the FtsZ ring in prokaryotic cytokinesis. *PLOS Comput. Biol.* **4**, e1000102 (2008). doi:10.1371/journal.pcbi.1000102 Medline

46. P. Mateos-Gil, A. Paez, I. Hörger, G. Rivas, M. Vicente, P. Tarazona, M. Vélez, Depolymerization dynamics of individual filaments of bacterial cytoskeletal protein FtsZ. *Proc. Natl. Acad. Sci. U.S.A.* **109**, 8133–8138 (2012). doi:10.1073/pnas.1204844109 Medline

47. N. Wiener, Generalized harmonic analysis. *Acta Math.* **55**, 117–258 (1930).

48. T. Baba, T. Ara, M. Hasegawa, Y. Takai, Y. Okumura, M. Baba, K. A. Datsenko, M. Tomita, B. L. Wanner, H. Mori, Construction of *Escherichia coli* K-12 in-frame, single-gene knockout mutants: The Keio collection. *Mol. Syst. Biol.* **2**, 2006.0008 (2006).

49. T. G. Bernhardt, P. A. de Boer, SlmA, a nucleoid-associated, FtsZ binding protein required for blocking septal ring assembly over chromosomes in *E. coli*. *Mol. Cell* **18**, 555–564 (2005). doi:10.1016/j.molcel.2005.04.012 Medline

50. M. Kitagawa, T. Ara, M. Arifuzzaman, T. Ioka-Nakamichi, E. Inamoto, H. Toyonaga, H. Mori, Complete set of ORF clones of *Escherichia coli* ASKA library (a complete set of *E. coli* K-12 ORF archive): Unique resources for biological research. *DNA Res.* **12**, 291–299 (2005). doi:10.1093/dnares/dsi012 Medline